Spectral and morphological characteristics of synthetic nanophase iron (oxyhydr)oxides

Elizabeth C. Sklute[1], **Srishti Kashyap**[2], **M. Darby Dyar**[1,3], **James F. Holden**[2], **Thomas Tague**[4], **Peng Wang**[4], and **Steven J. Jaret**[5]

[1]Department of Astronomy, Mount Holyoke College, 50 College St., South Hadley, MA 01075, USA

[2]Department of Microbiology, University of Massachusetts, N418 Morrill Science Center IV North, 639 N. Pleasant St., Amherst, MA 01003, USA

[3]Planetary Science Institute, 1700 East Fort Lowell, Suite 106, Tucson, AZ 85719-2395, USA

[4]Bruker Optics Inc., 19 Fortune Dr., Billerica, MA 01821, USA

[5]Department of Geoscience, Stony Brook University, 255 Earth and Space Science Building, Stony Brook, NY 11794-2100, USA

Abstract

Nanophase iron (oxyhydr)oxides are ubiquitous on Earth, globally distributed on Mars, and likely present on numerous other rocky solar system bodies. They are often structurally and, therefore, spectrally distinct from iron (oxyhydr)oxide bulk phases. Because their spectra vary with grain size, they can be difficult to identify or distinguish unless multiple analysis techniques are used in tandem. Yet, most literature reports fail to use multiple techniques or adequately parameterize sample morphology, making it difficult to understand how morphology affects spectral characteristics across techniques. Here, we present transmission electron microscopy, Raman, visible and near-infrared, and mid-infrared attenuated total reflectance data on synthetic, nanophase akaganéite, lepidocrocite, goethite, hematite, ferrihydrite, magnetite, and maghemite. Feature positions are tabulated and compared to those for bulk (oxyhydr)oxides and other nanophase iron (oxyhydr)oxides from the literature. The utility and limitations of each technique in analyzing nanophase iron (oxyhydr)oxides are discussed. Raman, mid-infrared, and visible near-infrared spectra show broadening, loss of some spectral features, and shifted positions compared to bulk phases. Raman and mid-infrared spectroscopies are useful in identifying and distinguishing akaganéite, lepidocrocite, goethite, and hematite, though ferrihydrite, magnetite, and maghemite have overlapped band positions. Visible near-infrared spectroscopy can identify and distinguish among ferrihydrite, magnetite, and maghemite in pure spectra, though akaganéite, lepidocrocite, and goethite can have overlapping bands. It is clear from this work that further understanding of variable spectral features in nanophase iron (oxyhydr)oxides must await

✉ Elizabeth C. Sklute ecsklute@mtholyoke.edu.

additional studies to robustly assess effects of morphology. This study establishes a template for future work.

Keywords

Nanophase iron (oxyhydr)oxides: nanophase akaganéite; nanophase lepidocrocite; nanophase goethite; nanophase hematite; ferrihydrite; nanophase magnetite; nanophase maghemite; Fourier transform infrared (FTIR) attenuated total reflectance (ATR) spectroscopy; Visible near-infrared (VNIR) spectroscopy; Raman spectroscopy

Introduction

It has become increasingly apparent that a substantial portion of natural iron (oxyhydr)oxides exist in a size regime that is much smaller than previously realized, often only tens of nanometers in one or more crystallographic directions (Braunschweig et al. 2013). These 'nanophase' (1–100 nm in at least one direction) iron (oxyhydr)oxides are likely involved in, and often the driving force for, many of Earth's surface processes (Wigginton et al. 2007; Hochella et al. 2008; Navrotsky et al. 2008; Braunschweig et al. 2013). They facilitate nutrient and contaminant transport, influence fluid chemistry and soil evolution, affect cloud formation and fault dynamics (Hochella et al. 2008), and are inextricably linked to life through the metabolic activity of microbes (Hansel et al. 2003; Hochella et al. 2008). In fact, iron redox cycling in a multitude of surface and subsurface environments is probably controlled by the bioavailability of nanoscopic iron phases (Roden 2003; Borch et al. 2010; Braunschweig et al. 2013). Nanophase iron (oxyhydr)oxides (iron NPOs) are also believed to be ubiquitous on Mars as part of the Martian dust (Bell et al. 2000; Morris et al. 2000, 2006; Klingelhoefer et al. 2006), and have been found in many achondrites (e.g., Burns and Fisher 1994), suggesting that they are present on the meteorites' source bodies. Given what we know of their prevalence and importance, iron NPOs are likely common phases on most rocky solar system bodies, where they affect (or drive) surface processes, and thus is it critically important that their spectral characteristics be well understood.

Nanophase compounds effectively bridge the gap between colloids and minerals (Wigginton et al. 2007; Delay and Frimmel 2012), displaying size-dependent properties that are distinct from bulk phases. Those properties do not always simply scale with increased surface area (Chernyshova et al. 2007; Wigginton et al. 2007; Hochella et al. 2008). Particularly when grain size is below ~15 nm, minerals with identical formulas display structural differences between bulk (>micrometer sized) particles and nanophase particles, as well as between nanophase samples with differing sizes (Chernyshova et al. 2007; Wigginton et al. 2007; Hochella et al. 2008). Increased curvature at the surface can make it impossible for crystal faces to fully develop. Steps, edges, and strain-induced surface and internal inhomogeneity cause these nanoscopic phases to display structural, and even chemical, differences from their bulk counterparts (see Gilbert and Banfield 2005 for an excellent discussion).

Such differences must lead to changes in spectral characteristics depending on the wavelength used, making spectral discrimination of iron NPOs much more challenging

(Chernyshova et al. 2007). Furthermore, nanophase iron (oxyhydr)oxides impose specific limitations on each common characterization method. Due to these complicating factors, multiple characterization techniques are required for definitive identification of nanophase samples (Wigginton et al. 2007); yet very few studies have used multiple spectroscopic techniques to analyze the *same* samples of iron NPOs with known grain morphologies (size, shape, crystallinity). Syntheses of iron (oxyhydr)oxides are notably difficult to precisely duplicate (Lewis and Schwertmann 1979; Schulze 1984) and the resulting slight structural changes lead to morphological and spectral changes (Lu et al. 2005; Heitjans et al. 2007; Liu et al. 2009; Rout et al. 2014). Thus, analyzing the same samples by multiple techniques is essential in developing links between morphology and spectral features. Furthermore, nanophase (and bulk) iron (oxyhydr)oxides transform readily between phases because stability is dependent upon storage conditions and surface area to volume ratio. Therefore, although there is a wealth of knowledge on trends in formation, stability, and conversion of iron (oxyhydr)oxide phases, many of which include extensive spectral data, very little of it can be used to investigate definitive links between spectral and morphological characteristics (size, shape, and crystallinity) in iron NPO samples. Without such knowledge, it is difficult to interpret spectral data from the surfaces of rocky solar system bodies where iron NPOs undoubtedly play important roles.

This study addresses gaps in the literature by investigating the same suite of synthetic, nanophase iron (oxyhydr) oxides using transmission electron microscopy (TEM) and visible and near-infrared (VNIR), mid-infrared (MIR), and Raman spectroscopy. Our overall goal is to clarify linkages between spectra and morphology, and to identify complementary techniques that can be used for *definitive* identification and discrimination of iron NPOs on Earth and other rocky solar system bodies. This paper is unique in that it employs all of these types of spectroscopy on the exact same set of samples, which have undergone minimal (and controlled) storage time. We focus on spectroscopic methods here because they are the most practical when studying remote sensing data and they are better able to detect small modal amounts of these phases than in situ XRD.

The current study seeks to present and discuss new reference VNIR, MIR, and Raman spectra of well characterized (by TEM) nanophase iron (oxyhydr)oxides, highlighting limitations and considerations in using and interpreting results from each analytic technique. Results lay the groundwork for in-depth studies that seek to understand the relationships among size, shape, crystallinity, synthesis method, and spectral properties for iron NPOs, ensuring consistent and robust identification.

Background

In this section, techniques used in this study are briefly reviewed to identify potential inconsistencies that may be encountered in literature reports on iron NPOs and to facilitate the acquisition of robust spectral and morphological data on iron NPOs.

Raman and infrared (IR) spectroscopy are highly complementary techniques that result predominantly from molecular vibrations caused by the interaction of the medium with incident radiation. Where IR spectroscopy probes the interaction with light that is absorbed,

Raman spectroscopy probes the interaction with light that is inelastically scattered (Raman scattering). These distinct phenomena lead to different selection rules for IR- or Raman-"active" vibrations. While IR-active vibrations change the dipole moment of the atomic arrangement in question (e.g., the asymmetric stretch of CO_2), Raman-active vibrations change the polarizability, or distribution of the electron cloud (e.g., symmetric stretch of CO_2) (Nasdala et al. 2004). Used together, information about atomic arrangements in a compound can be determined (such as the energy of Fe–O bonds in oxides). VNIR or ultraviolet–visible (UV–VIS) spectroscopies can then be used with them to look at electronic transitions that occur at shorter wavelengths (higher energies), creating a powerful set of techniques for identification and discrimination of many different compounds. Combining these spectroscopies with TEM can facilitate understanding of the link between morphology and its relationship to the energy of bonding environments (spectral features).

Phenomena associated with spectral changes in nanophase size domains can be understood by considering the energy of the bonds producing the features; as grain size decreases into the nanophase, strained surface domains become more energetically distinct from sites in the bulk crystal (Gilbert and Banfield 2005). Furthermore, the percentage of those domains relative to the bulk crystal sites increases; thus, these distorted surface sites become responsible for a greater contribution to the overall spectrum. The result is that the range of energies over which a vibrational transition may occur increases in most nanophase samples, thereby broadening spectral features. Although well-ordered nanophase samples can be created, increased distortion of the nanoparticle surface can propagate into the material (Gilbert and Banfield 2005). This disorder (often referred to as 'poorly crystalline') further increases the range of excitable bond energies and further broadens features. In the most extreme cases, the structural and, therefore, spectral character of surface domains begins to closely resemble other minerals; this is the case for very fine-grained hematite, whose surface domains become maghemite-like in the nanophase (de Grave et al. 1986), with the number of maghemite-like defects depending on grain size and reaction kinetics during formation (Chernyshova et al. 2007).

Another phenomenon affecting vibrational spectra of nanophase samples is sample hydration. As grain size decreases, the ratio of surface area to volume increases, so the relative amount of surface adsorbed water can increase significantly (Lu et al. 2005), adding hydration features to VNIR and MIR spectra.

The application of Raman spectroscopy (Nasdala et al. 2004) to the study of iron oxides is relatively new, in part because the fluorescence of iron compounds seen at many common Raman wavelengths may be confounding. A greater deterrent is that iron (oxyhydr)oxides readily change phase due to the heat of the Raman laser, converting almost invariably to hematite (Hanesch 2009), the most thermodynamically stable iron (oxyhydr)oxide. This transformation can be avoided by analyzing the sample in a fluid medium that disperses the laser heat. Raman issues can also be mitigated through the use of low laser power (2 mW) and very short integration times combined with high numbers of integrations, allowing heat to dissipate between each laser excitation, avoiding thermally induced changes or damage. For extremely sensitive samples, multiple spots can be analyzed, such that each spot sees minimal laser time, and the resultant spectrum is an average of the multiple spots. This last

method also averages any potential sample heterogeneity. When samples are fine-grained or poorly crystalline, signal to noise decreases, peaks broaden, and some peaks disappear entirely (cf. Jubb and Allen 2010). In all these ways, the use of Raman spectroscopy to study nanophase samples provides many, albeit surmountable, challenges.

The technique of IR spectroscopy is well covered by Stuart (2004), Farmer (1974), and King et al. (2004). Single crystal transmission IR (T-IR) spectroscopy can be subject to polarization effects that change the position and depth of spectral features (Wenrich and Christensen 1996). Powder T-IR spectroscopy, in which a sample is dispersed (assuming random orientation) in an IR-transparent medium, must be carried out on samples much smaller than the wavelength of light to avoid contributions from non-Rayleigh scattering. While this is not a problem for nanophase samples, comparisons between nanophase samples and literature bulk reports should be made cautiously because inadequately prepared bulk samples may display non-Rayleigh scattering contributions and/or alterations from the grinding process itself (crystal damage, water absorption, etc.; King et al. 2004). T-IR data for powdered samples may also contain a mixture of transverse and longitudinal optical modes that can give rise to changes in band minima, feature broadening, change of band shapes, additional "surface modes", and interference fringing (Decius and Hexter 1977; Mcmillan 1984; McMillan and Hofmeister 1988; King et al. 2004).

Emission spectroscopy, on the other hand, is most often performed on particles that are much larger than the wavelength of incident light to eliminate particle size effects (King et al. 2004). While this method produces spectra that are most directly comparable to remotely sensed data, spectral features change shape dramatically with decreasing particle size (King et al. 2004; Pan et al. 2015). Spectra of pressed pellets of fine-grained samples decrease surface reflections, better approximating larger-grained sample spectra (Salisbury and Wald 1992; Pan et al. 2015), but do not completely eliminate particle size effects (Pan et al. 2015).

Reflectance IR (R-IR) spectroscopy is a variable technique where the geometry of the source and detector creates conditions that can be appropriate for a wide variety of samples and experiments (bidirectional, directional-hemispheric, biconical a.k.a. diffuse reflectance, attenuated total reflectance). The resulting mixture of transmission, reflectance, and scattering varies with geometry, sampling depth, and surface characteristics. Quantitative analysis of the results depends on applying appropriate theoretical treatments to the data, which may in turn make assumptions about the refractive index, absorptivity, and/or grain size of the material depending on the type of experiment (King et al. 2004). *As a result, literature data on identical materials from different types of IR spectroscopy are often not directly comparable* (Parikh et al. 2014).

IR spectra of nanophase materials will generally display broadened features that can then become overlapped, which leads to the apparent loss of certain bands (cf. Lu et al. 2005; Serna and Morales 2004). In addition, surface-sorbed water increases in nanophase samples (Lu et al. 2005), as noted above. This leads to the appearance of hydration features in the sample spectra. Heating samples to remove this surface water can readily change the crystallinity or phase of iron NPOs, even with mild amounts of heat (Bosch et al. 2010); this fact is often exploited in studies on sample evolution (cf. Jacob and Abdul Khadar 2010).

Furthermore, drying of iron NPOs may cause structural changes because the solvent has a marked effect on the energy, and thus the structure, of the nanoparticle surface (Carlson and Schwertmann 1990; Kandori et al. 1998; Waychunas 2009). Because this surface region is a statistically significant portion of the particle for nanoscopic phases, drying can significantly impact the spectral properties. For applications where a dry surface is expected, then the dry product is likely the correct reference material, but drying techniques must be consistent. However, if the energetics of the surface in a wet environment are of interest, as would be the case for some biomineralization scenarios (Kashyap et al. 2016), then spectra of the hydrated surfaces are much more relevant. In light of these considerations, this paper presents IR results for freshly filtered samples (that resemble gels) using MIR attenuated total reflectance (ATR) spectroscopy. A later paper will compare IR characteristics of iron NPOs from different hydration conditions and drying techniques (Sklute et al. in preparation), which is a complex topic on its own.

VNIR electronic spectral contributions are well reviewed by Burns (1993) and Cornell and Schwertmann (2006). The NIR region in iron NPO spectra records hydration feature overtones and combination modes that can be swamped by increased hydration and the multiple energetic environments of the iron NPO structure. The VIS region where electronic transitions occur is also significantly impacted by grain size. This phenomenon was investigated in depth by Morris et al. (1989) for hematite, where spectral contrast in the VIS region declined significantly as grain size decreased, making identification more difficult. Finally, quantum confinement, which is the change in the electronic environment resulting from small material sizes, shifts electronic energy levels and changes the position of electronic absorptions in the UV–VIS spectrum (Gilbert and Banfield 2005). With VNIR spectroscopy, it is much more difficult to measure freshly filtered/gel samples because of the strength of water and hydroxyl features across this wavelength range. However, VNIR spectra are so useful in the study of dry iron oxides that they are crucial to include when spectrally parameterizing these materials, even if sample preparation differs.

This paper seeks to define VNIR, MIR, and Raman spectral characteristics of iron NPO's of well-defined sample morphology, a practice we hope other authors will adopt so that the effects of iron NPO morphology on spectral characteristics across techniques can be determined.

Methods

Sample synthesis

Eight iron NPOs were synthesized for this study: 2-line ferrihydrite (Fh), akaganéite (Ak102315), goethite (Goet011515 and Goet012315), lepidocrocite (Lep030415), hematite (Hem100915), maghemite (Magh061815), and magnetite (Mag060516). All glassware used in the following syntheses was acid washed to avoid impurities and trace contaminants.

1. Fh was synthesized after Lovley and Phillips (1986); a 0.4 M solution of $FeCl_3$ was slowly brought to pH 7 with NaOH under vigorous stirring. Each sample was then centrifuged (5000 G, 20 min) roughly three times with doubly de-ionized (DDI) 18 $M\Omega$ cm^{-1} water because excessive centrifugation causes a

transformation to hematite and this can be detected by a slight reddening of the sample. The sample was then re-suspended and stored at 4 °C. New samples of Fh were made continuously and have been found to be spectrally identical.

2. Akag102315 was synthesized after Schwertmann and Cornell (2000); 54.06 g $FeCl_3.6H_2O$ was dissolved in 2 L of DDI water. The glass flask was sealed and then reacted at 65 °C for 8 days. The sample was rinsed via centrifugation five times and then dialyzed for 8 days, changing water one time per day (using DDI water). The aqueous suspension was then stored at 4 °C.

3. Lep030415 was synthesized after Schwertmann and Cornell (2000); 11.93 g $FeCl_2.4H_2O$ was added to 300 mL N_2 purged water after which the pH was quickly adjusted to 6 with NaOH while stirring and with N_2 flowing. The N_2 was then replaced with air and the solution was oxidized through a frit at the lowest detectable rate (<50 mL min^{-1} using a Mathes 7200 flow meter) with automated addition of NaOH using a peristaltic pump to maintain pH of ~5.6 ± 0.05. The rate of base addition was adjusted so that acidification of the solution due to oxidation was well balanced by the base addition; the very end of the synthesis requires rapid base addition to maintain pH. The solution was oxidized until the pH remained stable (pH ~5.9). The sample was rinsed via centrifugation with DDI water, re-suspended, and then stored at 4 °C.

4. Hem100915 was synthesized after Schwertmann and Cornell (2000) but was scaled down by a factor of 10; 16.16 g $Fe(NO_3)_3$ was dissolved in 40 mL DDI water (1 M) and transferred to a titration burette. In a glass flask, 500 mL of DDI water was brought to a boil and the $Fe(NO_3)_3$ solution was added at a rate of 100 mL h^{-1} dropwise to the boiling solution. The sample was cooled overnight at room temperature, rinsed by centrifugation with DDI water, re-suspended and stored at 4 °C.

5. Goet011515 was synthesized after Schwertmann et al. (1985); 50 mL of 1 M $Fe(NO_3)_3$ was added to 450 mL of 1 M KOH (solutions made with DDI water) and then stored at 4 °C for 9 months. The sample was then rinsed by centrifugation using DDI water, re-suspended, and stored at 4 °C.

6. Geot012315 was synthesized after Schwertmann and Cornell (2000); 9.9 g of $FeCl_2.4H_2O$ was added to 1 L of N_2 purged DDI water, followed by 110 mL of 1 M $NaHCO_3$, after which the solution was slowly oxidized (lowest detectable flow) with air for 48 h. The sample was rinsed by centrifugation using DDI water, re-suspended, and stored at 4 °C.

7. Magh061815 was synthesized after Taylor and Schwertmann (1974); a 0.064 M $FeCl_3–FeCl_2$ solution with Fe^{2+}/Fe^{3+} of 9 was made with N_2 purged DDI water, to which a 1.2% NaOH (also N_2 purged) solution was added to adjust pH quickly to 7 with vigorous stirring and N_2 flowing. The solution was then slowly oxidized with air while the pH was automatically maintained at 7 ± 0.05 with NaOH using a peristaltic pump. For this synthesis, it is important to keep pH above 7, as goethite can form competitively at lower pH values. In addition,

carbon species in the oxidizing gas can lead to a goethite impurity but can be removed by bubbling the air through a strong NaOH solution. If oxidation is too fast, lepidocrocite can result. The solution was rinsed via centrifugation using DDI water, re-suspended, and stored at 4 °C.

8. Mag060516 was synthesized after Maich et al. (2012) with slight modifications; 8.6 mL of concentrated HCl was added to 200 mL of N_2 purged DDI water (0.5 M) with stirring and N_2 flowing in a 1000 mL flask closed by parafilm. Next, 9.95 g of $FeCl_2.4H_2O$ and then 27.06 g of $FeCl_3.6H_2O$ were added with stirring and N_2 flowing. A peristaltic pump was then used to slowly (to minimize overwhelming the fume hood with evolved gases) add N_2 purged 1 M NH_3OH to the parafilm-covered flask until the pH no longer changed (about 800–1000 mL; pH ~9.1). The sample was rinsed with N_2-purged water by magnetic decantation using a rare-earth disc magnet to produce settling at the bottom of a sealed storage container. After each rinse, N_2 was briefly bubbled through the solution before capping and settling (to minimize possible oxidation to maghemite). After the last wash, the sample was re-suspended in N_2-purged DDI water; the container was then N_2 sparged and was stored at 4 °C. Sample was removed from this container only in a glove box by syringe and the container was regularly re-sparged with N_2.

Aliquots of all samples except Mag060516 were freeze-dried for dry analysis, while the remainder was left in fluid suspension (Fig. 1). Mag060516 was dried in a glove box under N_2 directly prior to each dry analysis. Dry samples were stored at −80 °C to minimize phase changes.

Analysis

Directly after synthesis, all samples were confirmed to be pure phases at the resolution of XRD at the University of Massachusetts Amherst on a Philips X'PertPW3040-MPD diffractometer that uses Cu-Kα radiation and operates in Bragg–Brentano geometry. After all spectral data had been acquired, additional XRD patterns (collected on freshly filtered aliquots from the fluid suspensions dried under inert atmosphere) were measured to ensure samples had not changed phase over the timeframe of this study. Those XRD data were collected at Smith College on a Scintag XDS 2000 powder diffractometer (40 kV, 35 mA) using Cu-Kα radiation in Bragg–Brentano geometry. Samples were mounted on a quartz zero-background sample holder and run with 0.02 2Θ steps using integration times that ranged depending on each sample (acquisition usually took between 12 and 24 h). Mag060516, being air sensitive, was instead sent to the XRD facility in the MIT Department of Chemistry for XRD analysis under cryogenic conditions (http://web.mit.edu/x-ray/index.html). For TEM mounts, wet oxides were shaken and then allowed to partially settle. The dilute supernatant was then pipetted on to a 200-mesh formvar-coated, carbon-stabilized copper grid, allowed to settle for 1 min, and wicked dry with blotting paper. TEM were acquired at 80 kV on the Phillips CM 100 TEM at Mount Holyoke College (MHC), which is equipped with a 40–100 kV tungsten filament, single-tilt goniometer stage, and AMT digital camera (Fig. 2). Pixel sizes were calibrated using a catalase standard and individual grain

size ranges were determined using ImageJ (NIH, USA, http://rsb.info.nih.gov/ij/) with N 100.

Raman and MIR ATR spectra were collected at Bruker Optics in their demonstration facility (Billerica, MA). Raman spectra were collected on freshly filtered samples with a Bruker Senterra micro-Raman spectrometer using a 532 nm excitation laser and a 20× objective. Collection parameters depended on the sensitivity of the sample but laser power was typically 2 mW and each spectrum was generally an average of 20 10-s integrations. When samples showed any hematite peaks or appeared visually red after analysis, laser power was decreased to 0.2 mW and/or more spectra with shorter integration times were taken (this technique was also used to mitigate fluorescence). MIR ATR spectra were collected on freshly filtered samples with a Bruker Vertex 70 FTIR using a diamond ATR accessory. The spectrometer uses an ultra-wide range beamsplitter that covers 6000–30 cm^{-1}. An air-cooled SiC IR source and DTGS detector with a diamond window were used to facilitate acquisition over the full frequency range. Spectral resolution was set to 4 cm^{-1} and each spectrum was a 1-min integration using Norton Beer medium apodization.

VNIR spectra were collected in the Vibrational Spectroscopy Lab (Stony Brook University, Stony Brook, NY) using an ASD Fieldspec3 Max (3 nm resolution @ 700 nm) with incident angle, i, set to 30°, and emission angle, e, set to 0°. Before each measurement, the signal was optimized, a dark current spectrum was collected, and a white reflectance calibration to calibrated Spectralon was taken. Spectra were acquired on freeze-dried samples that had been stored at −80 °C (except for Mag060516). Each spectrum is an average of 100 1-s integrations and three spectra of each mineral were taken to check spectral stability.

Spectral analysis was carried out by baseline (for Raman) or continuum removed (for MIR and VNIR) spectra. Baseline removal for Raman was carried out using the top-hat algorithm (Perez-Pueyo et al. 2010). Continuum removal for MIR and VNIR spectra was performed both with the convex hull 'rubber band' baseline removal algorithm (Wartewig 2003) as well as in the program ENVI (http://www.harrisgeospatial.com/Product-sandSolutions/GeospatialProducts/ENVI.aspx). Peak positions were then determined by fitting a series of Gaussians or Lorentzians (for the rubber band processed samples) or with a Da Vinci script (for ENVI processed samples), which calculates the potential minima through the sign change in the channel to channel difference (used with a 10-channel boxcar filter). While both methods deliver peak positions where the error is well below the spectral resolution of the data set (and can, therefore be assumed to be the spectral resolution of the data set), these two protocols delivered different peak positions (by up to 20 cm^{-1} or 10 nm) due to the difference in continuum removal. The results reported here were compared to each other and to the unprocessed spectra to choose the most reasonable answer but because of the variability caused by continuum removal, errors are not reported on these numbers. Rather, all digital data are included as part of the supplemental material and posted on the Mineral Spectroscopy Laboratory website (Carey et al. 2017) for download and manipulation.[1]

---

[1]Data are currently available at http://www.nemo/cs/umass/edu:54321, which is a temporary site during construction. For the permanent website, please contact mdyar@mtholyoke.edu.

Results and interpretation

Imaging

TEM images of representative samples of synthetic iron NPOs are shown in Fig. 2, with grain size distributions shown in Fig. 3; crystallographic and physical parameters are given in Table 1. Morphologies and size ranges are quite distinct for the different species. Fh, Hem100915, and Mag060516 are composed of 3 nm, 6 nm, and 12 nm spheres, respectively, whereas Magh061815 is composed of 6 nm irregular spherical particles. Ak102315 and Goet01515 are well-formed lathes that are 41 and 7 nm wide, and 367 and 96 nm long, respectively. The second goethite sample, Goet012315 is composed of 3 nm wide (62 nm long), poorly crystalline lathes with ragged edges. Lep030415 is made up of thin, rectangular platelets that measure 31 by 237 nm. Most samples have fairly narrow size distributions. Ak102315 and Lep030415 show the largest deviations from their mean values. For Lep030415, this could be partially due to oriented aggregation (Soltis and Penn 2016) of smaller 'building blocks' into larger structures leading to both forms being present in the sample. All samples have the morphologies expected for the mineral and syntheses used to produce them.

Raman

Raman spectra for the synthetic iron NPOs are shown in Fig. 4. Positions of the Raman features are listed in Table 2 along with Raman data from the literature (Hanesch 2009; Das and Hendry 2011; Das et al. 2013), and the origin and symmetry of each Raman transition, where available (Bersani et al. 1999; Chamritski and Burns 2005; Jubb and Allen 2010; Rout et al. 2014). Despite the fact that these nanophase sample spectra were acquired using low laser power, all of the diagnostic and a majority of the expected Raman peaks are visible. Nanophase hematite, goethite, lepidocrocite, and akaganéite are all differentiable by Raman spectroscopy in this study. Although peak positions for hematite, goethite, akaganéite, and lepidocrocite are quite similar, the relative intensities of those peaks and overall shape of the spectra are distinct for these minerals in the nanophase state. In contrast, primary features for nanophase magnetite, maghemite, and ferrihydrite are highly overlapped. If these features are broadened due to decreased crystallinity or grain size, or mixed together, it is quite challenging to distinguish these phases by Raman spectroscopy alone. Furthermore, Raman features for the iron (oxyhydr) oxides are overlapped with those for iron-bearing sulfates (Sobron et al. 2014), although iron sulfates also display prominent sulfate vibrational features at >900 cm^{-1}, where iron NPOs are relatively featureless in this region. These facts, combined with the sensitivity of iron (oxyhydr)oxides to alteration during analysis, suggest that Raman spectroscopy should be used with care (and best in multi-technique studies) for the analysis of iron NPOs.

MIR

Mid-infrared ATR spectra (1550–50 cm^{-1}) are plotted in Fig. 5. Positions of MIR absorptions from 1200 to 200 cm^{-1} are listed in Table 3, along with the analogous MIR features for bulk oxides (Lewis and Farmer 1986; Murad and Bishop 2000; Barrón et al. 2003; Chamritski and Burns 2005; Cornell and Schwertmann 2006; Parikh et al. 2014; Bishop et al. 2015). Where available, site symmetry and participating atoms are given for

each absorption (Lewis and Farmer 1986; Murad and Bishop 2000; Barrón et al. 2003; Chamritski and Burns 2005; Cornell and Schwertmann 2006; Blanch et al. 2008; Parikh et al. 2014; Bishop et al. 2015). Full spectra to 6000 cm^{-1} are given in supplementary material 1. Only the abbreviated spectra are shown because these freshly filtered gels all show broad hydration features ~3200 cm^{-1}. Hydration in hydroxides has been studied at length (Schwertmann et al. 1985; Cambier 1986a; Weckler and Lutz 1998; Ruan et al. 2001). Due to the combination of sample hydration and grain size (leading to greater hydration), these iron NPOs display many hydration-associated features that may not be expected for the comparative bulk sample in question (e.g., bands appear at 779 cm^{-1} in hematite and 706 and 773 cm^{-1} in magnetite). In addition, some features expected for crystalline samples are not observed due to the small size. This is the case for the 400, 380, 303, and 310 cm^{-1} Fe–O vibrations often seen in crystalline hematite (Parikh et al. 2014), as well as for the 270 and 210 cm^{-1} Fe–O vibrations commonly observed in magnetite (Chamritski and Burns 2005).

Goethite is easily identified in the MIR through its pair of hydroxyl vibrations at 839 cm^{-1} (in plane; δOH) and 794 cm^{-1} (out of plane; γOH) (Parikh et al. 2014). While the values of δ_{OH} vibrations (883 cm^{-1}) in our nanophase samples are quite shifted, no other oxide displays such features in that wavelength range. The spectrum of Ak102315 does show two overlapping and asymmetric absorptions at 837 and 816 cm^{-1}, while Lep030415 has a single absorption at 741 cm^{-1}, but these can be easily differentiated. The isolated, asymmetric absorption at 634 cm^{-1} in Ak102315 allows it to be distinguished from the other iron NPOs. Even though a similar band position is seen in the nanophase goethites, that feature is part of a doublet for goethite samples.

According to Bishop et al. (2015), the most identifiable feature of lepidocrocite is an absorption at 1150 cm^{-1} from the in-plane hydroxyl bend (Bishop et al. 2015); however, we find the δ_{OH} absorption at 1018 cm^{-1} (bulk value) is more easily observed in mixed samples. No other iron (oxyhydr)oxide studied has features in the same location, though both features are close to the range of sulfate absorptions in sulfate-bearing minerals (Bishop et al. 2015; Lane et al. 2015). The γ_{OH} feature for lepidocrocite at 752 cm^{-1} is also frequently reported. Hematite, even hydrated Hem100915, does not display the hydroxyl vibrations of goethite and lepidocrocite. The absence of these features along with a prominent pair of absorptions at 525 and 443 cm^{-1} (Parikh et al. 2014; 518 and 433 cm^{-1} in Hem100915) make this mineral distinguishable from the other iron (oxyhydr)oxides. As with Raman spectroscopy, the spectral features for magnetite and maghemite are highly overlapped, especially in these highly hydrated samples. So while MIR spectroscopy is better able to differentiate ferrihydrite from magnetite and maghemite, it is anticipated that in spectra of mixed iron (oxyhydr)oxides, like those encountered in partially bioreduced samples of ferrihydrite (Sklute et al. 2016a), discrimination between these three phases would be quite difficult using MIR spectroscopy alone.

Several other factors should be considered when using MIR spectra to identify or differentiate iron NPOs. The first is that in vibrational spectroscopy, the assumption that lattice modes are size- and shape-independent only holds true if a sample axis is much greater than the phonon wavelength (Ruppin and Englman 1970; Rendón and Serna 1981). Therefore, the energy of a feature, which can vary between the longitudinal and transverse

frequencies, will depend on the crystallographic direction or plane in which the vibration occurs (Lewis and Farmer 1986) when crystal size is small. This means that samples with different shapes can have spectral features that are shifted (Rendón and Serna 1981; Lewis and Farmer 1986), complicating interpretation. Furthermore, peak positions may differ on the order of tens of wavenumbers between ATR/reflectance vs. transmission spectra (cf. Bishop et al. 2015). While the ATR spectra from this study are most directly comparable to diffuse reflectance (DRS or DRIFTS) spectra, band widths, depths, and peak ratios vary between the two methods (Parikh et al. 2014). In sum, spectral changes due to grain size, grain shape, and crystallinity must be carefully investigated in multiple configurations before general statements can be made about changes in spectral features with any given parameter (for more information on the causes of band variation between types of IR spectroscopy, see King et al. 2004).

VNIR

VNIR spectra for freeze-dried synthetic iron NPOs are displayed in Fig. 6. Literature parameters (Sherman and Waite 1985; Scheinost et al. 1998; Cornell and Schwertmann 2006; Bishop et al. 2015) along with assignments for band origins where available (Hunt et al. 1971; Scheinost et al. 1998; Cornell and Schwertmann 2006; Bishop et al. 2015) are listed in Table 4. Due to the fine-grained nature of the samples and because no effort was made to dehydrate the oxides (that could have changed phase or crystallinity), hydration features in the NIR can be seen in all spectra for all samples. This is particularly interesting for the oxide hematite, which shows hydration features ~1.43, 1.80, and 1.94 μm that are much more intense than in the hydroxides goethite and lepidocrocite. In addition to these 'extra' hydration features, VNIR spectra for several samples lack bands that are expected in larger-grained specimens. For example, several of the low wavelength Fe^{3+} spin-forbidden crystal field transitions for hematite at 0.380, 0.404, 0.444 μm, for maghemite at 0.434, 0.666, and 0.934 μm, and for goethite and lepidocrocite at 0.434 μm are not observed in these spectra.

Differentiation of bulk iron (oxyhydr)oxides using VIS spectral features is well covered by Scheinost et al. (1998) and our findings are generally consistent with theirs. Of the iron NPOs studied, hematite has the lowest wavelength absorption in the 0.8–0.9 μm range ($^6A_1$-$^4T_1$). The position of this absorption and the inflection at ~0.55 μm have been used to distinguish hematite from other iron (oxyhydr)oxides (Morris et al. 1985; Scheinost et al. 1998). Akaganéite is occasionally reported to have a similar 0.908 μm feature (Cornell and Schwertmann 2006 and references therein), but the position of its inflection is lower (0.502 μm). It is also the only sample surveyed that displays a sharp absorption in the >2.2 μm region, a feature that may make it identifiable in a mixed spectrum. While our ferrihydrite sample did not display many of the VIS absorptions reported by Scheinost et al. (1998), ferrihydrite displays a characteristic sharp OH absorption at ~1.40 μm on the slope to its NIR maximum. This sets ferrihydrite apart from the other iron (oxyhydr)oxides. While goethite can be clearly variable between syntheses, the position of the VIS absorptions and the VIS maximum make it generally differentiable from the other iron NPOs using this technique. Finally, VNIR spectroscopy is particularly useful in distinguishing nanophase magnetite from maghemite, where other methods struggle. Pure, end-member nanophase

magnetite is almost entirely spectrally flat, while nanophase maghemite has a broad VIS maximum (0.726 μm for Magh061815). These differences make the two minerals easily separable in pure samples.

All vibrational features in the NIR region result from the first overtone of the OH stretching mode (~1.4 μm) and combination bands of "free" water and hydroxyl and are, therefore, not considered diagnostic for iron (oxyhydr) oxides (Hunt et al. 1971). The positions of these features are listed in Table 4 and a review of their origins can be found in Hunt and Salisbury (1970).

A parameter that is not directly associated with an absorption process, but that is occasionally reported in the literature, is the VIS maximum (cf. Morris et al. 1985). For ferrihydrite, the VIS maximum is 0.801 μm. For Goet012315 and Goet011515, the VIS maxima are 0.763 and 0.757 μm, respectively. Interestingly, only Goet011515, the more crystalline sample, displays the second local maximum of 0.597 μm. Lepidocrocite also displays two maxima at 0.794 and 0.623 μm and akaganéite has a single VIS maximum at 0.728 μm. While magnetite, Mag060516, was almost entirely featureless, maghemite, Magh061815, has a VIS spectral maximum of 0.726 μm. Finally, Hem100915 displays a VIS maximum at 0.746 μm.

Discussion

While the bulk spectral properties of iron (oxyhydr)oxides are generally consistent from sample to sample, the spectral properties of nanophase samples can vary based on grain size, shape, crystallinity, and preparation method as explained above. In the ensuing discussion, it quickly becomes apparent that results that are inconsistent among disparate studies may sometimes be explained by variations in grain size or analysis technique. While the extent of this variation is not yet well-known, it is clear that the most robust comparisons and identifications of iron NPOs would proceed from libraries of complete sets of spectral data taken *on the same well-constrained samples with known grain sizes/morphologies*. This study lays the groundwork for the creation of such a library.

The power of such a study is demonstrated by the work of Morris, Golden, Bell and co-authors (Morris et al. 1985, 1989, 1991, 1997, 2000; Morris and Lauer 1990; Golden et al. 1994; Bell et al. 1995) who investigated a small suite of sub-micron and nanophase, synthetic oxides. This set of papers applied diffuse reflectance VNIR, T-MIR, and Mössbauer spectroscopies to a series of "sub-micron" synthetic industrial pigment powders of hematite, maghemite, magnetite, goethite, and lepidocrocite, along with truly nanophase hematite precipitated in the pores of silica or alumina, where both the pore size and the matrix material particle size were varied. Due to its breadth, this data set has been used extensively in the study of Martian surface materials (Morris et al. 2000; Bell et al. 2000; Christensen et al. 2000; Lane et al. 2002; Arvidson et al. 2005; Glotch and Kraft 2008; Johnson et al. 2016), thus showing the utility of comprehensive spectral data on identical samples in the interpretation of planetary surface processes. However, the sub-micron samples, when nanophase, are on the high end of the nanophase size range (size effects become enhanced below 15 nm), and only a few of the pore-deposited hematites were

analyzed by multiple spectroscopic techniques. In addition, the magnetite samples are cation deficient, and akaganéite was not included.

There is ample literature on the bulk characteristics of iron (oxyhydr)oxides, which are succinctly reviewed in the section on iron oxides in Parikh et al. (2014) and more comprehensively in the book by Cornell and Schwertmann (2006) that summarizes decades of experimental results on iron (oxyhydr)oxides. While some of the samples presented in the latter are technically nanophase, they are not presented as such in that text, so grain size information for the specific samples in question is not always included. The book does not include Raman spectra of bulk oxides (although band positions from Oh et al. (1998) are reported), but Raman for bulk (oxyhydr)oxides are well summarized by Das and Hendry (2011), Jallad and Ben-Amotz (2001), and the in-depth computational study by Chamritski and Burns (2005).

Akaganéite

Raman

In this study, our ~41 × 367 nm Ak102315 has prominent Raman peaks at 316 and 391 cm^{-1}, which are shifted from those for 'bulk' akaganéite at 307 and 387 cm^{-1} (Das and Hendry 2011; grain size unknown). Mohapatra et al. (2010) synthesized ~18 × 90 nm akaganéite and found that the prominent Raman peaks appeared at 310 and 380 cm^{-1}, with two weaker features at 490 and 700 cm^{-1}. Ak102315 shows comparable features at 546 and 723 cm^{-1} but these are a better match to the 'bulk' features at 535 and 719 cm^{-1}. Given this limited data set, there is no clear trend in peak position with grain size.

MIR

In the MIR, Ak102315 (~41 × 367 nm) can be identified by an asymmetric δ_{OH} absorption at 634 cm^{-1} with a shoulder at 677 cm^{-1}. Our nanophase results are comparable to those of Šari et al. (1998), who synthesized several nanophase akaganéite samples with crystallite sizes of 7–9 nm × ~100 nm. The reported T-MIR data for their samples showed absorptions at ~637–645 cm^{-1} and 667–696 cm^{-1}. Deliyanni et al. (2001) also reported T-MIR data for synthetic 2–6 nm akaganéite, in which this feature was recorded at 688 cm^{-1} without an attempt to make out a shoulder. All these values are comparable to the two ATR MIR absorptions reported for 'bulk' akaganéite of 644 and 698 cm^{-1} by Bishop et al. (2015), who unfortunately did not report dimensions for their samples. Although akaganéite is thought to be a mineral that always has a nanophase dimension (Bishop et al. 2015), the exact sizes for most of the samples examined in that paper were not given. One sample was analyzed by TEM in 1979 (Murad 1979) and by various forms of IR spectroscopy in Murad and Bishop (2000). At that time, that sample was ~200 × 1600 nm. Another sample from Sherman et al. (1982) is noted to be 150 nm long, which would imply that the width is <100 nm, but no other information is given. Moreover, it is unclear whether Oswald ripening may have had an effect in changing grain sizes of those samples in the intervening years. Because transmission data are not directly comparable to ATR data, it is difficult to draw any conclusions about peak position with respect to synthesis method or grain morphology for the samples were size is well constrained.

VNIR

In the VNIR, Ak102315 (~41 × 367 nm) shows Fe^{3+} spin-forbidden crystal field transitions at 0.387, 0.428, 0.512, 0.650, and 0.970 μm. The $^6A_1$-$^4T_1$ absorption at 0.970 μm in our sample is substantially higher than that reported for 'bulk' akageneite in Cornell and Schwertmann (2006) or Bishop et al. (2015), who charted this feature at 0.91 and 0.92 μm, respectively. Because the Cornell and Schwertmann sample was of unspecified grain size and the Bishop et al. (2015) samples could have undergone Oswald ripening over the last ~35 years, it is unclear what exactly causes such a significant variation in the position of this spectral feature. Despite this anomaly, the VIS maxima for Ak102315 and the Bishop et al. (2015) samples are both 0.73 μm. Continuum removal may play a part in explaining these discrepancies, as it would shift the apparent band minimum within each band. As mentioned above, akaganéite is the only iron NPO that displays a strong NIR absorption >2.2 μm. In Ak102315, this feature is at ~2.452 μm, consistent with that of the bulk sample at 2.47 μm.

Lepidocrocite

Raman

The distinguishing Raman feature for our lepidocrocite (~31 × 237 nm, with pH controlled at 5.6) is observed in Lep030415 at 253 cm^{-1}, consistent with the reported 'bulk' value of 250 cm^{-1} (Hanesch 2009; grain size unknown). The Hanesch sample was produced by the same method as that employed here (described in Schwertmann and Cornell 2000), although the pH may have been higher, leading to a larger-grained, more crystalline product. Das et al. (2013) also used the same Schwertmann and Cornell (2000) synthesis method and reported using a near neutral pH (for a more crystalline product) and SEM shows their lepidocrocite to be >100 nm in two directions, although the thickness of the lathes is still nanophase (~3.3 nm). Their Raman analysis put the position of the main lepidocrocite feature at 248 cm^{-1}. They also reported features at ~214, 305, 374, 520, and 645 cm^{-1}. Lep030415 does not display features ~214, 305, or 520 cm^{-1} and the other features are slightly shifted to 378, 527, and 648 cm^{-1}. Because the data are so limited and there are no clear trends, it is not yet possible to theorize about a link between grain size and Raman peak position in this mineral.

MIR

The prominent MIR absorptions used for identification in Lep030415 (~31 × 237 nm) occur at 11567, 1020, and 741 cm^{-1} consistent with those for the 'bulk' (50 × 50 × 500 nm) sample of Lewis and Farmer (1986) at 1150, 1018, and 752 cm^{-1}. Unfortunately, that paper does not specify what type of IR spectroscopy was performed on the samples; therefore, no further comparison is attempted. Ristić et al. (2006) provide T-MIR spectra of a lepidocrocite that by SEM seems to be nanophase in at least one direction; however, specific grain size information is not included. The IR bands for their sample are 1157 and 1021 cm^{-1}. Maiti and Sujatha Devi (2015) report T-MIR data for a synthetic nanophase lepidocrocite with a hydrodynamic diameter of 154 nm. However, while they show this sample (S3) to be an XRD match to only lepidocrocite, their MIR spectrum shows signs of goethite contamination through prominent hydroxyl absorption features at 890 and 798 cm^{-1}. *This is a prime example of an instance where XRD does not provide sufficient resolution to confirm*

a pure product. Bell et al. (1995) report the T-MIR absorptions for a 30×900 nm lepidocrocite at 1159, 1020, and 752 cm^{-1}. Sheydaei and Aber (2013) synthesized nanophase sulfate-bearing lepidocrocite with a size of 21 nm using XRD line broadening and ~30×250 nm using TEM. Their MIR results show absorptions at 1153, 1019, and 749 cm^{-1} but they do not stipulate what type of MIR spectroscopy was used. Given the scarcity of complete data, it is impossible to draw any meaningful conclusions at this time.

VNIR

Lepidocrocite has five well-documented Fe^{3+} spin-forbidden crystal field transitions at 0.359, 0.434, 0.485, 0.649, and 0.961 μm in 'bulk' samples (Sherman and Waite 1985; grain size unknown). The $^6A_1\rightarrow^4E^4A_1$ at ~0.43 μm is not observable in our sample (~31×237 nm) and the position of the other features is shifted to 0.414, 0.482, 0.726, and 0.978 μm. The VIS maxima for Lep030415 cannot be compared to the Sherman and Waite (1985) data because those authors do not report that values; however, Morris et al. (1985) give VIS maxima for the 30×900 nm acicular sample also examined in Bell et al. (1995). They report two maxima at 0.621 and 0.822 μm, compared to our Lep030415 of 0.623 and 0.794 μm. For comparison, their sample displayed absorptions at 0.393, 0.463, 0.704, and 0.982 μm. The physical cause of the substantial shift in several of these features is unclear at this time.

Goethite

Raman

Goethite is most distinguishable in Raman spectra through its peak at 385 cm^{-1} (Hanesch et al.; grain size unknown). While many of the goethite peaks are overlapped with hematite peaks (albeit with different relative intensities), this Fe–O/-OH feature is sufficiently offset from hematite's Fe–O peak at 412 cm^{-1}. In our samples, Goet011515 (~7×96 nm) and Goet012315 (~3×62 nm), this feature occurs at 395 and 397 cm^{-1}, respectively (still sufficiently offset from our hematite's 408 cm^{-1} feature). Zhang et al. (2016) synthesized nanophase goethites of different shapes: ~30 nm nanospheres, ~50 nm wide nanorods, nanosheets of unspecified thickness, and a bulk/aggregate sample. Their Raman spectra for those samples were almost identical, with this feature appearing at 391 cm^{-1}. Zhang et al. (2016) state that they believe their samples to all be highly crystalline, leading to the consistency of values, however, inspection of their spectra show a prominent doublet at 218 and 281 cm^{-1}, and a low, broad peak at 391 cm^{-1}. While some of their values are closest to those for goethite, the overall spectral shape and the feature at 218 cm^{-1} (hematite is identified by a strong peak at 225 cm^{-1}) is much more reminiscent of hematite. Due to the overlapping feature positions between these two minerals, a final assessment cannot be made but it seems likely that their samples were transformed during Raman analysis. Ayachi et al. (2015) synthesized hematite through goethite. While the size and shape of the goethite are not provided, it is presumably similar to the $300 \times 100 \times 10$ nm plates of the hematite made from it. Using low laser power, they collected a Raman spectrum of the goethite and the position of the main identification feature for their sample was 387 cm^{-1}. While the substantially different crystallinities of our two samples do not appreciably change the position of the Raman peaks, the significantly less crystalline sample, Goet012315, shows much less intensity in some of the smaller peaks. In fact, the features at ~250 and 483 cm^{-1}

almost disappear. Unfortunately, there are not sufficient data to assess the role of grain size on goethite's Raman spectral features.

MIR

In the MIR, goethite is easily identified, even at low concentrations, by its hydroxyl absorptions at 839 cm^{-1} (in plane) and 794 cm^{-1} (out of plane) (Parikh et al. 2014; ATR; grain size unknown). Goet011515 (~7×96 nm) and Goet012315 (~3×62 nm) have similar out-of-plane hydroxy deformations at 788 and 796 cm^{-1}, respectively, but have a significantly shifted in-plane hydroxyl deformation at 883 cm^{-1} for both samples. Interestingly, the Fe–O and Fe–OH vibrations of our samples do not substantially deviate from those for the bulk sample of Parikh et al. (2014) but speculation is not possible without additional morphological information on the bulk sample. A set of nanophase goethites (Series 39) across a range of sizes and crystallinities synthesized and originally analyzed by Schwertmann et al. (Schwertmann 1984a; Schwertmann et al. 1985) were also investigated via T-MIR by Schwertmann et al. (1985) and Cambier (1986b). These samples varied in synthesis temperature and annealing temperature, and displayed grain size- and crystallinity-dependent shifts in their T-MIR spectra. For the unannealed samples, as the crystal height and width increased from 9 and 38 nm to 52 and 108 nm, respectively, δ_{OH} increased from 884.9 to 889.9 cm^{-1} and γ_{OH} increased from 791.0 to 794.0 cm^{-1} (Schwertmann et al. 1985). For this set of samples, the strongest correlation was between crystal width and γ_{OH} ($R^2 = 0.885$). For annealed samples, as height and width increased from 9 and 38 nm to 33 and 68 nm, respectively, δ_{OH} increased from 884.9 to 893.5 cm^{-1} and γ_{OH} increased from 791.0 to 795.1 cm^{-1}. For this series, the strongest correlation was between sample height and δ_{OH} ($R^2 = 0.921$). The sizes given in this study were determined from XRD line broadening and, therefore, represent the size of the scattering domain rather than the crystal size, and lathe length was not assessed by this method, but TEM was presented for some of the samples (Schwertmann et al. 1985).

Bell et al. (1995) report T-MIR absorptions of 904 and 796 cm^{-1} for a 50×400 nm sample and 908 and 798 cm^{-1} for a 100×700 nm sample, fitting the general trend that larger samples have higher wavenumber absorptions, but not falling in the expected range of Series 39 samples. Žic et al. (2007) synthesized a set of goethites under a range of chemical and temperature conditions. 0ne of their samples, S14, is clearly nanophase (~50 nm in one direction) in their SEM images, and has T-MIR hydroxyl absorptions at 894 and 797 cm^{-1}. However, the other highly aggregated and larger-grained goethite samples had similar parameters. Kosmas et al. (1986) synthesized goethite by a variety of methods with a range of crystal sizes (determined by XRD line broadening and fiber-optic Doppler anemometry (F0DA)) and shapes (lathes of different widths). The hydroxyl absorptions for those samples ranged from 887 to 894 cm^{-1} for δ_{OH} and 792–799 cm^{-1} for γ_{OH} with the strongest correlation between sample width and γ_{OH} ($R^2 = 0.819$). Cwiertny et al. (2009) investigated nanorods (7×81 nm) and microrods (25×670 nm) and found that the ATR spectra of the two samples showed slight differences in the position of the δ_{OH} and γ_{OH} features. The nanorods absorbed at 897 and 796 cm^{-1} while the microrods absorbed at 892 and 794 cm^{-1}. The authors note that this is opposite the trend observed by Cambier (1986a, b). The samples analyzed by Schwertmann and Cambier (Schwertmann Series 39), however, were

synthesized under identical chemical conditions and only temperature was varied. Many of the multi-sample goethite studies, including ours, used different chemical conditions for the production of each sample. Clearly, the relationship between spectral features in the MIR for this mineral and grain size does display a trend but it is not completely straightforward and requires more detailed and systematic research.

VNIR

Goethite has five reported Fe^{3+} spin-forbidden crystal field transitions in 'bulk' spectra at 0.364, 0.434, 0.480, 0.649, and 0.917 μm (Sherman and Waite 1985; grain size unknown). Scheinost et al. (1999), however, their in-depth study of the diffuse reflectance spectra of Al-substituted goethites identified a sixth transition (an additional electron pair transition of unspecified value). Neither of our samples show the $^6A_1\rightarrow^4E_4A_1$ transition at 0.434 μm, and several of the other transitions are shifted. For Goet011515 (~7 × 96 nm) and Goet012315 (~3 × 62 nm), respectively, the $^6A_1\rightarrow^4E$ transition occurs at 0.374 and 0.395 μm, the $^6A_1\rightarrow^4T_2$ transition occurs at 0.678 and 0.675 μm, the $^6A_1\rightarrow^4T_1$ transition occurs at 0.968 and 0.957 μm. While the variation in the $^6A_1\rightarrow^4T_2$ transition may be due to the continuum removal procedure, the other two are clearly shifted to higher wavelengths for our nanophase samples. Several of the goethites studied via MIR (above) also included VNIR or UV-VIS spectral data. Morris et al. (1985) provide VNIR reflectance data for samples in Bell et al. (1995) and find absorptions at 0.381, 0.445, 0.652, and 0.932 μm for their 50 × 400 nm sample and at 0.417, 0.447, 0.645, and 0.896 μm for their 100 × 700 nm sample. Kosmas et al. (1986) also included the position and intensity of the second derivative of the reflectance spectrum ~0.485 μm and Munsell parameters for their goethite samples. The position of this second derivative was found to be consistent between the end-member goethites in their study but shifted with Al substitution. Ayachi et al. (2015) included UV–VIS spectra of their precursor goethite (~300 × 100 × 10 nm) and note the position of the 2($^6A_1\rightarrow^4T_1$) transition is at 0.495 μm, higher than either of our finer-grained samples. Cwiertny et al. (2009) included UV–VIS of suspensions of their nanorods (7 × 81 nm) and microrods (25 × 670 nm) but only report absorption maxima, which are not directly comparable to reflectance minima. Howwever, they show a shift to lower wavelengths for the larger sample.

Finally, Zhang et al. (2011) looked at UV–VIS spectra of nanophase goethites of several sizes to determine the change in band gap. Their samples sizes, determined via XRD (Rietveld analysis), were 8.7, 10.1, 16.6, 26.8, and 38.2 nm. They also included TEM of all samples which show sample sizes to be ~10 × 30 nm for the 8.7 nm sample, ~10 × 100 nm for the 10.1 nm sample, ~20 × >200 nm for the 16.6 nm sample, ~25 × 400 for the 26.8 nm sample and ~100 × 300 nm for the 38.2 nm samples. The authors note that aggregation makes it difficult to truly assess the particle boundaries from TEM. Their Gaussian fits to the UV–VIS absorbance spectra (200–700 nm) give up to eight overlapping bands, with five bands in the wavelength range covered in our analyses. Their samples showed a systematic trend for all bands >0.30 μm, where the wavelength of the transition increased as particle size increased. Because absorbance and reflectance spectra are not directly comparable, it is difficult to fit our results into this trend. While the Zhang et al. (2011) study is compelling, more detailed work comparing UV-VNIR spectral features to grain size and shape is required to fully understand this relationship.

The VIS maxima for Goet011515 (~7 × 96 nm) and Goet012315 (~3 × 62 nm) are 0.757 and 0.763 μm respectively. These are relatively close to those reported by Morris et al. (1985) of 0.759 μm (100 × 700 nm) and 0.761 μm (50 × 400 nm). In both cases, the larger sample has a lower VIS maximum. Morris et al. (1985) report a second, local maximum for their samples at 0.585 μm. Interestingly, only Goet011515, the more crystalline sample, displays the second local maximum of 0.597 μm.

Hematite

Nanohematite is one of the most commonly studied iron NPOs because it can crystallize into myriad structures of many sizes. Thus, there is an enormous body of literature, of which only a few highlights are given here, in which a synthesis was confirmed using one or more spectroscopic techniques.

Raman

Raman spectra of bulk hematite possess a characteristic peak at 225 cm^{-1} (Hanesch 2009; grain size unknown); however, the peak at 412 cm^{-1} is also not overlapped with any other iron (oxyhy)droxide investigated. Our sample, Hem100915 (~6 nm spheres), shows these peaks at 226 and 408 cm^{-1}. Dar and Shivashankar (2014) synthesized nanoparticulate hematite through the conversion of magnetite, through maghemite. One of the two hematite samples (60 nm spheres) was analyzed by Raman spectroscopy and showed the 'identification' peaks at 225 and 407 cm^{-1}. Jubb and Allen (2010) used vapor deposition to create ~50 and ~250 nm thick polycrystalline thin films of hematite. Their reported values for the 'identification' peaks were 229 and 414 cm^{-1}, with the thicker sample having a slightly higher wavenumber peak ~229 cm^{-1}. Li et al. (2012) exposed 10 nm magnetite nanoparticles to the Raman laser until they converted to hematite, with peaks at 219 and 398 cm^{-1}. The same magnetite was also converted to hematite by annealing and the peaks appeared at 223 and 410 cm^{-1} for that sample, which was presumably slightly larger grained due to the annealing process. Ayachi et al. (2015) analyzed their hematite final product (300 × 100 × 10 nm) by Raman spectroscopy and reported hematite 'identification' peaks at 219 and 401 cm^{-1}.

Chernyshova et al. (2007) performed a detailed study of the shift in Raman peak position with size (7, 37, and 120 nm) and synthesis method in hematite and found that the A_{1g} peak at ~226 cm^{-1} is more stable to changes in grain size than the E_g at 412 cm^{-1}. They report that the Raman peaks broaden and shift to lower wavenumbers with decreasing particle size but give no experimental values. In contrast, the limited data set from our study does not seem to always follow this trend. In addition, because the reported values of Jubb and Allen (2010) and Ayachi et al. (2015) are systematically shifted to higher and lower wavenumbers, respectively (including undiscussed peaks), it is possible that their Raman spectrometers were not properly calibrated, a problem which may be prevalent in the earlier literature.

MIR

In the MIR, 'bulk' hematite can be identified by a pair of Fe–O vibrations at 525 and 443 cm^{-1} (Parikh et al. 2014; ATR; grain size unknown). In our sample, Hem100915 (~6 nm

spheres), these absorptions occur at 518 and 433 cm^{-1}, respectively. Chernyshova et al.'s (2007) in-depth analysis of the factors affecting the position of these two features, including the anticipated effect of surface modes and grain shape on the contributions of the transverse and longitudinal optical modes in each band, concluded that the E_u absorption ~460 cm^{-1} is more stable against shape effects than the A_{2u}/E_u band ~550 cm^{-1} but that the interaction of size and shape is not straightforward and that kinetic effects due to synthesis methods also play a part. However, for their samples (18, 39, and 120 nm), the E_u T-MIR absorption fit to a core/shell pair at ~440/~475 cm^{-1}, trends towards lower wavenumbers and broader bands for finer-grained samples. In addition, due to the increased intensity in the low wave-number feature with decreased grain size, along with other evidence from the literature, they conclude that this band is due to a poorly crystalline or proto-hematite component. Lu et al. (2005) also presented a detailed study of the change in hematite MIR spectral parameters with grain size. They looked at finite size effects of four samples of nanophase hematite annealed at different temperatures (maintaining similar shapes). While their sizes are derived from XRD patterns (more appropriately scattering domain size than grain size), they show there is definite link between grain size and T-MIR band position which is dependent upon if the vibrational mode is parallel or perpendicular to the c-axis. Like Chernyshova et al. (2007), they observed two components to each absorption feature investigated here, but concluded that absorptions at 440 and 630 cm^{-1} were from vibrations polarized parallel to c, and those at 480 and 540 cm^{-1} from vibrations polarized perpendicular to c. Decreased size caused the perpendicular modes to systematically shift to lower wave-numbers, eventually leading to a collapse of the 480 and 440 cm^{-1} absorptions into a single feature; however, specific values for these peaks were not provided. Rendón and Serna (1981) had previously investigated this effect in the T-MIR properties of nanophase hematite produced by heating nanophase goethite at different temperature, thereby producing different shapes (in-particle de-hydroxylation vs. sintering). They concluded that the absorptions at 645 and 400 cm^{-1} are caused by vibrations parallel to c, that absorptions at 525 and 440 cm^{-1} are from vibrations perpendicular to c, and that the shoulder at ~470 cm^{-1} was due to a surface vibration from a non-lathe component because it only increased in intensity for larger, sintered samples. The low-temperature, 80×400 nm lathes absorbed at 440 and 525 cm^{-1}. When heated further, thus sintering together, they found the absorption at ~525 cm^{-1} moved to higher wavenumbers, the same trend observed by Lu et al. (2005). Their trend with respect to the features at 440/470 cm^{-1} is more difficult to unravel but appears to show the same collapse for finer-grained samples. The authors also note that crystallinity does not change the position of MIR absorption, only size and shape do.

In addition to the in-depth studies reviewed above, Jubb and Allen (2010) show that in T-MIR spectra of their thin films (polycrystalline ~50 and ~250 nm thick films), hematite's 'identifying' absorptions appear at 440 and 526 cm^{-1}. Kosmas et al. (1986) synthesized hematite by a variety of methods with a range of crystal sizes (determined by XRD line broadening and FODA). The strongest correlation was found between XRD-derived size and the absorption ~570 cm^{-1} ($R^2 = 0.828$). Šari et al. (1998) reported T-MIR absorptions from their one pure hematite sample (50–100 nm spheres) as 480 and 575 cm^{-1}. Huang et al. (2011) synthesized nanoflowers of hematite (50–150 nm) composed of nanoflakes, and T-MIR absorptions were found to appear at 476 and 582 cm^{-1}. Wang and Gao (2010)

synthesized nanophase hematite of different shapes (~48 nm pseudo hexagonal and slightly larger hexagonal particles). Using an unspecified type of IR, they found all their samples absorbed at 470 and 564 cm^{-1}. Li et al. (2012) annealed ~10 nm magnetite particles and produced similarly sized (presumably slightly larger) hematite. Their hematite sample had T-MIR absorptions at 462 and 544 cm^{-1}. Mohammadikish (2014) investigated a set of nanophase hematites created at different temperatures and with different cook times. Only two are explicitly sized, 37 and 44 nm by XRD (consistent with TEM), but the SEM of the remaining samples show similar grain sizes. As synthesis temperature increased, one T-MIR 'identification' absorption stayed at 474 cm^{-1} but the other decreased from 555 to 548 cm^{-1}. However, one sample in that group is anomalous in both trends and the two high temperature samples have peaks at ~827 and 752 cm^{-1}, reminiscent of goethite. Finally, Bell et al. (1995) report on three nano-phase hematites (50×400 nm, 100×700 nm, and 1–4 nm hematite deposited in 6 nm pores of 28 nm silica spheres; the rest of their samples are either not nanophase or do not have reported spectral parameters) with T-MIR parameters of 444 and 525 cm^{-1} for the 50×400 nm sample and 447 and 528 cm^{-1} for the 100×700 nm sample, remaining consistent with the trend outlined above. However, their pore-deposited sample showed absorptions at 465 and 590 cm^{-1}, indicating a possible matrix effect on spectral parameters. Due to the different MIR experimental configurations, it is difficult to determine how our samples fall into this framework but we see no evidence of a high wavenumber shoulder in our ATR spectra or those of Parikh et al. (2014). It is worth noting that the Parikh et al. (2014) diffuse reflectance spectra place these absorptions at 578 and 480 cm^{-1}. While the MIR work on hematite is extensive, it remains incomplete and slightly conflicted. Here too, a rigorous and in-depth study of size and shape using different types of MIR spectroscopy would shed light on the complicated interplay between morphology and spectral features.

VNIR

Bulk hematite displays six Fe^{3+} spin-forbidden crystal field transitions in the VNIR at 0.380, 0.404, 0.444, 0.529, 0.649, and 0.884 μm (Sherman and Waite 1985; grain size unknown). Our nanophase hematite, Hem100915 (~6 nm spheres) only shows three of these bands: $2(^6A_1 \rightarrow {}^4T_1)$ at 0.537 μm, $^6A_1 \rightarrow {}^4T_2$ at 0.672 μm, $^6A_1 \rightarrow {}^4T_1$ at 0.881 μm. Zeng et al. (2007) synthesized hematite nanorods of different sizes (~20–40 $\times$ 40–800 nm) and showed that the $^6A_1 \rightarrow {}^4T_2$ absorption ~0.400 μm shifts from 0.386 μm for ~25 $\times$ 45 nm rods to 0.396 μm for ~25 $\times$ 450 nm rods to 0.408 μm for ~35 $\times$ 750 nm rods, thus changing the band gap energy. Ayachi et al. (2015) recorded UV–VIS spectra of their precursor hematite (~300 $\times$ 100 $\times$ 10 nm) and note the position of the $2(^6A_1 \rightarrow {}^4T_1)$ transition is at 0.550 μm. Kosmas et al. (1986) included the position and intensity of the second derivative of the reflectance spectrum ~0.660 μm and Munsell parameters for their hematite samples. Unlike the MIR data, the XRD-derived grain sizes do correlate with the second derivative value such that smaller grained samples have lower wavelength feature position (albeit over a very small range). Morris et al. (1985) provide VNIR reflectance data on the Bell et al. (1995) samples (excluding the pore-deposited sample). Those two samples show absorptions at 535, 0.639, and 0.861 μm for the 50×400 nm sample and 0.535, 0.634, and 0.854 μm for the 100×700 nm sample. Finally, Zhang et al. (2013) synthesized nanophase hematite of different shapes (~100 $\times$ 400 nm spindles, ~120 $\times$ 180 nm ellipsoids, ~100 nm spheres, and ~100 nm cubes)

and show that the VIS spectra of the different shapes are quite distinct. Although they only include band gap, not absorption position, it is worth mentioning to reflect that particle shape is a significant contributor to VNIR spectral characteristics.

Morris et al. (1985) also provide VIS maxima for their samples at 0.744 and 0.746 μm for the smaller and larger samples, respectively. Hem100915 displays a VIS maximum at 0.746 μm. While this data set is not large enough to draw any conclusions, it does show that UV-VNIR peak positions in nanophase hematite are dependent upon both particle size and shape and that further work is warranted to understand this relationship.

Magnetite and maghemite

Studies of nanophase magnetite are ubiquitous throughout the biomedical literature (Pankhurst et al. 2003; Zhong and Du 2003; Gupta and Gupta 2005; Maity and Agrawal 2007). Unfortunately, the compound produced is often simply referred to as magnetic nanophase iron oxide, with sparse attempts to characterize whether it is magnetite or maghemite. A notable exception is Maity and Agrawal (2007), who concluded that the synthesis procedures most often used to create magnetic nanoparticles (which assume that magnetite is the end product) actually seem to be producing maghemite. This confusion is partially due to the fact that nanophase magnetite and maghemite are extremely difficult to differentiate (Sklute et al. 2016b). This problem is one of the driving forces behind the current study, though a great deal more work is required to fully parameterize structural and spectral differences of nanophase magnetite and maghemite. Many of the studies listed below discuss products intended to be magnetite that may not be the actual end-member phase, a common problem with the literature.

Raman

Bulk magnetite and maghemite can be differentiated in Raman spectra through a peak at 670 cm^{-1} for magnetite vs. two peaks at 665 and 730 cm^{-1} in maghemite. In addition, magnetite can show lesser peaks at 540 and 310 cm^{-1} compared to lesser features in maghemite at 512 and 350 cm^{-1} (Hanesch 2009; grain size unknown). Our nanophase samples Mag060516 (~12 nm) and Magh061815 (~6 nm) do not show either of the lesser features. While the position of our magnetite's peak is consistent with that of bulk magnetite at 670 cm^{-1}, our nanophase maghemite has peaks at 673 and 709 cm^{-1}. This is noteworthy because ferrihydrite's identification peak falls at 716 cm^{-1} (Hanesch 2009), meaning that a mixture of nanophase magnetite and ferrihydrite may be difficult to distinguish from nanophase maghemite using Raman spectroscopy. Dar and Shivashankar (2014) synthesized two nanophase magnetites of ~30 and ~37 nm. Their Raman measurements show peaks at 330, 537, and 663 cm^{-1} for the 30 nm asymmetric particles. Jubb and Allen (2010) created polycrystalline ~40 and ~200 nm thin films of magnetite and polycrystalline ~50 and ~230 nm thin films of maghemite by vapor deposition. Their magnetite samples had Raman peaks at 310, 554, and 672 cm^{-1} while their maghemite samples had Raman peaks at 365, 511, and 700 cm^{-1}, with the 45 nm maghemite film showing appreciable intensity in only the highest wavenumber peak. While those Raman spectra for maghemite seem to be lacking one reported peak, the literature seems to support the occurrence of one broad feature at ~700 cm

$^{-1}$ (de Faria et al. 1997). Those authors note that the Raman peak positions for maghemite are dependent upon vacancy distribution and preparation method. Li et al. (2012) synthesized ~10 nm magnetic nanoparticles that were then annealed at different temperatures. The initial vacuum dried sample had a prominent Raman peak at 670 cm^{-1}. Under 2.58 mW laser power, the sample converted to maghemite with peaks at 704, ~660, 499, and 360 cm^{-1}. The maghemite sample created by annealing magnetite had the same peak positions except the lowest wavenumber peak shifted to 370 cm^{-1}. Based on the above studies, there is no apparent correlation between particle size and Raman shift. It is interesting, however, that the one sample reported to be non-spherical has a much different Raman shift for its main peak.

MIR

In the MIR, bulk magnetite and maghemite are differentiable by the position of Fe–O vibrations that occur in magnetite at 560 cm^{-1} (Chamritski and Burns 2005 from Gasparov et al. 2000; R-MIR data; large single crystal) and in maghemite at 553 and 440 cm^{-1} (Chamritski and Burns 2005). Mag060516 (~12 nm) absorbs at 547 cm^{-1} and Magh061815 (~6 nm) absorb at 541 and 433 cm^{-1}. Li et al. (2012) synthesized ~10 nm magnetite particles with a T-MIR peak at 572 cm^{-1} with a shoulder at 700 cm^{-1}. After mild annealing, the sample was believed to convert into maghemite and displayed absorptions at 572, 635, and 692 cm^{-1}; however, these seem more consistent with a mixed magnetite-maghemite phase. Bell et al. (1995) analyzed one of the three maghemites (50 × 300 nm) in Morris et al. (1985) by T-MIR and found absorptions at 553 and 442 cm^{-1}. Jubb and Allen (2010) also analyzed their polycrystalline ~50 and ~230 nm thin films of maghemite and polycrystalline ~40 and ~200 nm thin films of magnetite by T-MIR. The thicker maghemite film showed absorptions at 550 and 440 cm^{-1}, where the thinner film only showed one absorption at 546 cm^{-1}. The high absorptivity of the magnetite films only made it possible to observe a feature at 560 cm^{-1} in the spectrum of the thinner film. Maiti and Sujatha Devi (2015) synthesized maghemite with hydrodynamic diameters of 126 and 142 nm (not strictly nanophase) and report T-MIR absorptions for both samples at 449, 583, and 632 cm^{-1}, quite different from our sample or bulk literature reports. Serna and Morales (2004) synthesized an extensive set of maghemites through other oxides and a variety of direct methods and investigated the effects of shape and symmetry on mineral properties. While they include MIR data for the entire suite of samples, only a few peaks on three spectra are reported. The authors conclude that the IR results show ordering in maghemite occurs around 5 nm and that this can be seen by the gradual resolution of two broad peaks at 600 and 450 cm^{-1} for a 3.5 nm sample to substantial structure including peaks at 694, 640, 558, and 440 cm^{-1} in 12 nm particles. Garcia-Casillas et al. (2012) investigated the IR properties of magnetite synthesized in three different ways to form 16, 27, and 200 nm spherical particles. The 16 and 27 nm samples were believed to have slight cation deficiency based on their unit cell parameters. But because it is known from nanophase hematite that unit cell parameters can change with grain size (Lu et al. 2005), it is unclear if the use of unit cell parameter is an accurate method for differentiating the magnetite from maghemite. The 16 and 27 nm samples each showed two broad IR absorptions with reported minima of 606 cm^{-1}/441 cm^{-1} and 606 cm^{-1}/438 cm^{-1}, respectively. The 200 nm sample had more fine structure and showed absorptions at 606, 575, and 451 cm^{-1}. Neither the Serna and Morales (2004) nor the Garcia-Casillas et al.

(2012) study reports the type of MIR spectroscopy used, making it difficult to interpret these results. Because ordering seems to play an important role in the number and position of Raman peaks (and thus probably MIR absorptions as well), and full data sets are limited, no conclusions can be drawn about grain size vs. MIR spectral features at this time.

VNIR

As previously discussed, VNIR spectra of nanophase magnetite and maghemite are almost featureless. Bulk maghemite is, however, reported to have four Fe^{3+} spin-forbidden crystal field transitions at 0.434, 0.510, 0.666, and 0.934 μm (Sherman and Waite 1985). Magh061815 (~6 nm) only shows one absorption at 0.472 μm. Reports of VNIR spectral parameters for nanophase maghemite and magnetite are not forthcoming in the literature. An exception is the work by Morris et al. (1985), which reports the VNIR parameters for three nanophase maghemites seen in Bell et al. (1995): 0.488, 0.672, 0.919 μm (50 × 300 nm), 0.492, 0.634, 0.926 μm (90 × 600 nm), and 0.488, 0.630, 0.937 μm (70 × 300 nm). The first sample has a VNIR spectrum unlike those of the other two or our sample but has similar absorption values to the other two Morris et al. (1985) samples, with appreciable NIR reflectance. Morris et al. (1985) also reported VIS maxima for those samples of 0.776, 0.783, and 0.781 μm, respectively. Magh061815 has a much lower VIS maximum at 0.726 μm. The difference could be due to grain size or vacancy distribution, but more work is required to fully understand those relationships.

Ferrihydrite

Even though there are several 'forms' of ferrihydrite (2-, 3-, and 6-line), they are all found to have the same local structure; the XRD pattern differences are merely due to differences in the size of the scattering domain (Michel et al. 2007). While ferrihydrite is a mineral that always occurs in the nanophase (~2–10 nm; Michel et al. 2007), literature reports rarely size the particles as they are often at the resolution limit for many TEMs. Natural ferrihydrites show that 50–500 nm aggregates are common (Carlson and Schwertmann 1981; Schwertmann and Fischer 1973). For the purpose of this discussion, however, it is assumed that the size range of ferrihydrite is well within the error of sizes for many of the other iron NPOs and, therefore, will be treated as one size.

Raman

Synthetic 2-line ferrihydrite is reported to have one major peak at 707 cm^{-1} and two weaker peaks at 508 and 361 cm^{-1} (Das et al. 2013). In synthetic 6-line ferrihydrite, these bands appear at 710, 510, and 370 cm^{-1} (Hanesch 2009). In natural 2-line ferrihydrite, the band ~710 cm^{-1} is often the only one visible (Hanesch 2009). Our sample, Fh (2-line) only displays one Raman peak at 716 cm^{-1}.

MIR

Cornell and Schwertmann (2006) list the MIR absorptions in ferrihydrite as 450 and 650 cm^{-1}, of which the absorption at 450 cm^{-1} is diagnostic. They attribute both of these to deformation modes of OH, in contrast to the Fe–O vibrations seen in other oxides in this spectral range. Our ferrihydrite sample (~3 nm spheres) shows absorptions at 278, 434, 602,

and 698 cm^{-1}. Literature reports on the MIR spectral properties below 800 cm^{-1} are sparse making a full comparison difficult; however, Hausner et al. (2009) lists absorptions of 420, 480, 570, and 700 cm^{-1} for 6-line ferrihydrite. Their two-line ferrihydrite shows one broad absorption that seems to span the 700–570 cm^{-1} feature of their 6-line sample. Differences among the various studies are difficult to understand and data are lacking to reconcile them.

VNIR

In the VNIR, ferrihydrite displays up to four Fe^{3+} spin-forbidden crystal field transitions. Scheinost et al. (1998) lists the average positions of these for 22 synthetic and natural samples at 0.410, 0.492, 0.716, and 0.972 μm. The range for each transition was 0.386– 0.410 μm for $^6A_1{\rightarrow}^4E^4A_1$, 0.484–0.499 μm for $2(^6A_1{\rightarrow}^4T_1)$, 0.698–0.734 μm for $^6A_1{\rightarrow}^4T_2$, and 0.947–0.990 μm for $^6A_1{\rightarrow}^4T_1$ Our synthetic ferrihydrite only displays one absorption at 0.966 μm, well within the range for the $^6A_1{\rightarrow}^4T_1$ transition. VNIR spectral parameters for ferrihydrite are also sparse in the literature. Bishop and Pieters (1995) report a single absorption at ~0.92–0.93 μm, slightly outside the range of Scheinost et al. (1998). They also list a VIS maximum of 0.80 μm, consistent with our finding of 0.801 μm.

Conclusions

The discussion above comes from a literature review that is extensive but not comprehensive. Of the hundreds of articles on iron NPOs reviewed, only those cited here contain sufficiently detailed data to be listed in this comparison. The articles that were included in spite of their deficiencies were used to exemplify the incomplete reporting practices that confound the problem of linking morphological to spectral characteristics.

This study is important because the syntheses and analyses of iron NPOs reported here are novel in their completeness (multi-temperature Mössbauer data were also acquired for each sample but will be covered in their own paper). In addition, this work includes archived and complete digital data that can be included in spectral libraries used to investigate a multitude of planetary processes. Future studies following this model could greatly improve our understanding of the relationship between iron NPO morphology and spectral characteristics. It also makes clear where further work is needed to relate spectral features to grain sizes, facilitating ties back to paragenetic information. Use of spectroscopy to infer grain size and constrain formation mechanisms of nanophase iron (oxyhydr)oxides is highly desirable, given the relative ease and unequivocal identifications that can be obtained using suites of different types of spectroscopy. Spectroscopy may provide better species identification with far better detection limits than XRD. Moreover, spectroscopic methods are far easier to acquire in remote locations by orbiter or in situ rover. Finally, to extend these identifications to the natural systems where iron NPOs are prevalent (see Wigginton et al. 2007 and Braunschweig et al. 2013 for detailed information on these systems), to determine the role they play in those systems, and to understand the role of organic matter in iron NPO formation, structure, and stability, it is important to create a foundation using thorough and methodical studies of synthetic samples.

Accurate identification of type, size, crystallinity, and variation of iron (oxyhydr)oxides has significant implications for the surface processes in which they participate and the

conditions through which they crystallize. For example, ferrihydrite commonly forms through the hydrolysis of Fe^{3+} salts, while lepidocrocite and feroxyhyte form from Fe^{2+} salts (Vodyanitskii 2010). Ferrihydrite will convert into hematite under arid conditions, and can do so through a solid state transformation, whereas ferrihydrite converts into goethite through dissolution/reprecipitation, and, therefore requires hydration (Cornell and Schwertmann 2006). Silicic acid preserves ferrihydrite, inhibiting goethite formation (Cornell and Giovanoli 1987; Cornell et al. 1987; Wada and Ueno 2001). Si and Al can both inhibit lepidocrocite formation, with Al favoring the transformation of ferrihydrite to goethite over lepidocrocite (Vodyanitskii 2010) but hematite over goethite (Lewis and Schwertmann 1979). Substitution of Al will cause goethite to crystallize as shorter particles, which are less soluble (and therefore less reactive) than similarly sized particles of pure goethite (Schwertmann 1984b). The crystallinity and morphology of hematite particles depend on the properties of original phase (Liu et al. 2009) as well as the temperature of conversion (Yariv and Mendelovici 1979; Rendón and Serna 1981), where higher temperatures lead to more crystalline products (Yariv and Mendelovici 1979). Defect-containing hematites can be "healed" through subsequent thermal treatment (Wolska and Schwertmann 1989; Lu et al. 2005); so the identification of a poorly crystalline hematite or goethite has substantial information about the history of the materials. Clearly, spectral discrimination of these products will have a marked impact on the interpretation of surface processes on Earth and other rocky bodies.

Furthermore, while iron (oxyhydr)oxide spectral changes with grain size, grain shape, metal substitution, and crystallinity are well known, these changes are amplified in the nanophase size regime. The potentially large variation in the spectral properties of iron NPOs caused by the combination of size and analysis technique means that great lengths must be taken to ensure correct and robust phase identifications are made with remote sensing spectral data. The most important recommendations of the work are as follows:

- XRD peak positions will change with grain size because of changing unit cell parameters. Therefore, magnetite and maghemite should not be identified by XRD alone. In addition, XRD line width may not be a satisfactory method for determining grain size in these small and potentially disordered particles, and caution should be used when interpreting literature reports where XRD is the only method for particle size determination. Furthermore, XRD resolution is often insufficient to identify minor contaminants.

- Raman spectroscopy can cause phase changes in iron NPO samples, so low laser powers must be used, and nanophase magnetite, maghemite, and ferrihydrite have similar Raman spectra.

- MIR band positions change depending on the configuration of the MIR experiment (transmission, emissivity, reflectance) as well as with grain size, grain shape, and inclusions. In addition, nanophase samples hydrate, bands broaden, and magnetite and maghemite can be difficult to distinguish.

- Cornell and Schwertmann (2006) say that VNIR spectra are unreliable for differentiation between many iron oxides. While this statement is generally true due to the subtlety of features and band position and intensity changes due to

grain size, crystallinity, and substitution, VNIR may be a reliable method for differentiating magnetite from maghemite. However, VNIR is best performed on dried samples and drying may change phase and crystallinity.

While the challenges of phase identification in nanophase iron (oxyhydr)oxides are many, the application of some or all of these techniques in tandem can provide sufficient evidence for the identification and discrimination of iron NPOs. Results of this work also shed light on the paucity of integrative spectral studies that would facilitate such accurate identifications or unravel the effects of particle morphology on spectral properties. This project lays the groundwork for creation of a reliable spectral library for a comprehensive set of techniques. These are needed not only for definitive identification of iron NPOs, but also to provide additional information on grain size, shape, and crystallinity that potentially constrain deposition conditions and other information on (oxyhydr)oxide parageneses.

Supplementary Material

Refer to Web version on PubMed Central for supplementary material.

Acknowledgements

References

Arvidson RE, Poulet F, Bibring JP, Wolff M, Gendrin A, Morris RV, Freeman JJ, Langevin Y, Mangold N, Bellucci G (2005) Spectral reflectance and morphologic correlations in eastern Terra Meridiani, Mars. Science 307:1591–1594 [PubMed: 15718425]

Ayachi AA, Mechakra H, Silvan MM, Boudjaadar S, Achour S (2015) Monodisperse alpha-Fe_2O_3 nanoplatelets: synthesis and characterization. Ceram Int 41:2228–2233

Barrón V, Torrent J, de Grave E (2003) Hydromaghemite, an intermediate in the hydrothermal transformation of 2-line ferrihydrite into hematite. Am Mineral 88:1679–1688

Bell J, Roush T, Morris R (1995) Midinfrared transmission spectra of crystalline and nanophase iron–oxides oxyhydroxides and implications for remote-sensing of mars. J Geophys Res Planet 100:5297–5307

Bell JF, McSween HY, Crisp JA, Morris RV, Murchie SL, Bridges NT, Johnson JR, Britt DT, Golombek MP, Moore HJ et al. (2000) Mineralogic and compositional properties of Martian soil and dust: results from Mars Pathfinder. J Geophys Res Planet 105:1721–1755

Bersani D, Lottici PP, Montenero A (1999) Micro-Raman investigation of iron oxide films and powders produced by sol–gel syntheses. J Raman Spectrosc 30:355–360

Bishop J, Pieters C (1995) Low-temperature and low atmospheric-pressure infrared reflectance spectroscopy of Mars soil analog materials. J Geophys Res Planet 100:5369–5379

Bishop JL, Murad E, Dyar MD (2015) Akaganéite and schwertmannite: spectral properties and geochemical implications of their possible presence on Mars. Am Mineral 100:738–746

Blanch AJ, Quinton JS, Lenehan CE, Pring A (2008) The crystal chemistry of Al-bearing goethites: an infrared spectroscopic study. Mineral Mag 72:1043–1056

Borch T, Kretzschmar R, Kapple A, Van Cappellen P, Ginder-Vogel M, Voegelin A, Campbell K (2010) Biogeochemical redox processes and their impact on contaminant dynamics. Environ Sci Technol 44:15–23 [PubMed: 20000681]

Bosch J, Heister K, Hofmann T, Meckenstock RU (2010) Nanosized iron oxide colloids strongly enhance microbial iron reduction. Appl Environ Microb 76:184–189

Braunschweig J, Bosch J, Meckenstock RU (2013) Iron oxide nanoparticles in geomicrobiology: from biogeochemistry to bioremediation. New Biotechnol 30:793–802

Burns R (1993) Origin of electronic spectra of minerals in the visible and near-infrared region In: Pieters CM, Englert PAJ (eds) Remote geochemical analysis: elemental and mineralogical composition. Cambridge University Press, Cambridge, pp 3–30

Burns R, Fisher D (1994) Nanophase mixed-valence iron minerals in meteorites identified by cryogenic Mössbauer-spectroscopy. Hyperfine Interact 91:571–576

Cambier P (1986a) Infrared study of goethites of varying crystallinity and particle-size. 1. Interpretation of OH and lattice vibration frequencies. Clay Miner 21:191–200

Cambier P (1986b) Infrared study of goethites of varying crystallinity and particle-size. 2. Crystallographic and morphological-changes in series of synthetic goethites. Clay Miner 21:201–210

Carey C, Dyar MD, Boucher T, Giguere S (2017) Web-based software for preprocessing, matching, fitting, prediction, and visualization of spectroscopic data: the data exploration, visualization, and analysis of spectra (DEVAS) website. In: Proceedings of the 48th lunar and planetary science conference, 1097

Carlson L, Schwertmann U (1981) Natural ferrihydrites in surface deposits from Finland and their association with silica. Geochim Cosmochim Acta 45:421–429

Carlson L, Schwertmann U (1990) The effect of CO_2 and oxidation rate on the formation of goethite versus lepidocrocite from an Fe(II) system at pH-6 and pH-7. Clay Miner 25:65–71

Chamritski I, Burns G (2005) Infrared- and Raman-active phonons of magnetite, maghemite, and hematite: a computer simulation and spectroscopic study. J Phys Chem B 109:4965–4968 [PubMed: 16863155]

Chernyshova IV, Hochella MF, Madden AS (2007) Size-dependent structural transformations of hematite nanoparticles. 1. Phase transition. Phys Chem Chem Phys 9:1736–1750 [PubMed: 17396185]

Christensen PR, Bandfield JL, Clark RN, Edgett KS, Hamilton VE, Hoefen T, Kieffer HH, Kuzmin RO, Lane MD, Malin MC et al. (2000) Detection of crystalline hematite mineralization on mars by the thermal emission spectrometer: evidence for near-surface water. J Geophys Res Planet 105:9623–9642

Cornell R, Giovanoli R (1987) The influence of silicate species on the morphology of goethite (alpha-FeOOH) grown from ferrihydrite ($5Fe_2O_3.9H_2O$). J Chem Soc Chem Commun 6:413–414

Cornell RM, Schwertmann U (2006) The iron oxides: structure, properties, reactions, occurrences and uses. Wiley, New York

Cornell R, Giovanoli R, Schindler P (1987) Effect of silicate species on the transformation of ferrihydrite into goethite and hematite in alkaline media. Clay Clay Miner 35:21–28

Cwiertny DM, Hunter GJ, Pettibone JM, Scherer MM, Grassian VH (2009) Surface chemistry and dissolution of alpha-FeOOH nanorods and microrods: environmental implications of size-dependent interactions with oxalate. J Phys Chem C 113:2175–2186

Dar MI, Shivashankar SA (2014) Single crystalline magnetite, maghemite, and hematite nanoparticles with rich coercivity. RSC Adv 4:4105–4113

Das S, Hendry MJ (2011) Application of Raman spectroscopy to identify iron minerals commonly found in mine wastes. Chem Geol 290:101–108

Das S, Hendry MJ, Essilfie-Dughan J (2013) Adsorption of selenate onto ferrihydrite, goethite, and lepidocrocite under neutral pH conditions. Appl Geochem 28:185–193

de Faria DLA, Silva SV, de Oliveira MT (1997) Raman microspectroscopy of some iron oxides and oxyhydroxides. J Raman Spectrosc 28:873–878

de Grave E, Persoons R, Chambaere D, Vandenberghe R, Bowen L (1986) An Fe-57 Mössbauer-effect study of poorly crystalline gamma-FeOOH. Phys Chem Mineral 13:61–67

Decius JC, Hexter RM (1977) Molecular vibrations in crystals. McGraw-Hill, New York

Delay M, Frimmel FH (2012) Nanoparticles in aquatic systems. Anal Bioanal Chem 402:583–592 [PubMed: 22038580]

Deliyanni EA, Bakoyannakis DN, Zouboulis AI, Matis KA, Nalbandian L (2001) Akaganéite-type beta-FeO(OH) nanocrystals: preparation and characterization. Microporous Mesoporous Mater 42:49–57

Farmer VC (1974) The Infrared spectra of minerals Mineralogical society monograph 4. Mineralogical Society, Twickenham

Garcia-Casillas PE, Gonzalez CAR, Pérez CAM (2012) Infrared spectroscopy of functionalized magnetic nanoparticles In: Theophile T (ed) Materials science, engineering and technology, InTech, Rijeka, pp 405–420. http://www.intechopen.com

Gasparov LV, Tanner DB, Romero DB, Berger H, Margaritondo G, Forro L (2000) Infrared and Raman studies of the Ver-wey transition in magnetite. Phys Rev B 62:7939–7944. doi:10.1103/PhysRevB. 62.7939

Gilbert B, Banfield JF (2005) Molecular-scale processes involving nanoparticulate minerals in biogeochemical systems. Rev Mineral Geochem 59:109–155

Glotch TD, Kraft MD (2008) Thermal transformations of akaganéite and lepidocrocite to hematite: assessment of possible precursors to Martian crystalline hematite. Phys Chem Miner 35:569–581

Golden DC, Morris RV, Ming DW, Lauer HV, Jr (1994) High resolution transmission electron microscopy (HRTEM) of nanophase ferric oxides. In: Proceedings of the 25th lunar and planetary science conference, 1219

Gupta AK, Gupta M (2005) Synthesis and surface engineering of iron oxide nanoparticles for biomedical applications. Biomaterials 26:3995–4021 [PubMed: 15626447]

Hanesch M (2009) Raman spectroscopy of iron oxides and (oxy) hydroxides at low laser power and possible applications in environmental magnetic studies. Geophys J Int 177:941–948

Hansel CM, Benner SG, Neiss J, Dohnalkova A, Kukkadapu RK, Fendorf S (2003) Secondary mineralization pathways induced by dissimilatory iron reduction of ferrihydrite under advective flow. Geochim Cosmochim Acta 67:2977–2992

Hausner DB, Bhandari N, Pierre-Louis A-M, Kubicki JD, Strongin DR (2009) Ferrihydrite reactivity toward carbon dioxide. J Colloid Interface Sci 337:492–500 [PubMed: 19560780]

Heitjans P, Masoud M, Feldhoff A, Wilkening M (2007) NMR and impedance studies of nanocrystalline and amorphous ion conductors: lithium niobate as a model system. Faraday Discuss 134:67–82 [PubMed: 17326563]

Hochella MF, Lower SK, Maurice PA, Penn RL, Sahai N, Sparks DL, Twining BS (2008) Nanominerals, mineral nanoparticles, and earth systems. Science 319:1631–1635 [PubMed: 18356515]

Huang X, Guan J, Xiao Z, Tong G, Mou F, Fan X (2011) Flower-like porous hematite nanoarchitectures achieved by complexation–mediated oxidation–hydrolysis reaction. J Colloid Interface Sci 357:36–45 [PubMed: 21353233]

Hunt GR, Salisbury JW (1970) Visible and near-infrared spectra of minerals and rocks; I. Silicate minerals. Mod Geol 1:283–300

Hunt GR, Salisbury JW, Lenhoff CJ (1971) Visible and near-infrared spectra of minerals and rocks; III. Oxides and hydroxides. Mod Geol 2:195–205

Jacob J, Khadar MA (2010) VSM and Mössbauer study of nanostructured hematite. J Magn Magn Mater 322:614–621

Jallad KN, Ben-Amotz D (2001) Chemical imaging of iron oxides and oxyhydroxides using near-infrared Raman imaging microscopy. Mater Sci Technol Ser 17:1479–1486

Johnson JR, Bell JF, Bender S, Blaney D, Cloutis E, Ehliviann B, Fraeman A, Gasnault O, Kinch K, Le Mouelic S et al. (2016) Constraints on iron sulfate and iron oxide mineralogy from ChemCam visible/near-infrared reflectance spectroscopy of Mt. Sharp basal units, Gale Crater, Mars. Am Mineral 101:1501–1514

Jubb AM, Allen HC (2010) Vibrational spectroscopic characterization of hematite, maghemite, and magnetite thin films produced by vapor deposition. ACS Appl Mater Interfaces 2:2804–2812

Kandori K, Nakamoto Y, Yasukawa A, Ishikawa T (1998) Factors in the precipitation medium governing morphology and structure of haematite particles in forced hydrolysis reaction. J Colloid Interface Sci 202:499–506

Kashyap S, Sklute EC, Holden JF, Dyar MD (2016) Characterization of nanophase iron oxides produced through bioreduction by hyperthermophiles. In: Proceedings of the 47th lunar and planetary science, 2192

King PL, Ramsey MS, McMillan PF, Swayze GA (2004) Laboratory Fourier transform infrared spectroscopy methods for geologic samples. Short Course Ser Mineral Assoc Can 33:57–91

Klingelhoefer G, Morris RV, Yen AS, Ming DW, Schroeder C, Rodionov D (2006) Mineralogy on Mars at Gusev Crater and Meridiani Planum as seen by iron Mössbauer spectroscopy. Geochim Cosmochim Acta 70:A325–A325

Kosmas C, Franzmeier D, Schulze D (1986) Relationship among derivative spectroscopy, color, crystallite dimensions, and Al substitution of synthetic goethites and hematites. Clay Clay Miner 34:625–634

Lane MD, Morris RV, Mertzman SA, Christensen PR (2002) Evidence for platy hematite grains in Sinus Meridiani, Mars: Platy hematite grains in Sinus Meridiani, Mars. J Geophys Res Planet 107:9–1–9–15

Lane MD, Bishop JL, Dyar MD, Hiroi T, Mertzman SA, Bish DL, King PL, Rogers AD (2015) Mid-infrared emission spectroscopy and visible/near-infrared reflectance spectroscopy of Fe-sulfate minerals. Am Mineral 100:66–82

Lewis D, Farmer V (1986) Infrared-absorption of surface hydroxyl-groups and lattice-vibrations in lepidocrocite (gamma-FeOOH) and boehmite (gamma-AlOOH). Clay Miner 21:93–100

Lewis D, Schwertmann U (1979) Influence of Al on iron-oxides. 3. Preparation of Al goethites in M-KOH. Clay Miner 14:115–126

Li Y-S, Church JS, Woodhead AL (2012) Infrared and Raman spectroscopic studies on iron oxide magnetic nano-particles and their surface modifications. J Magn Magn Mater 324:1543–1550

Liu H, Li P, Lu B, Wei Y, Sun Y (2009) Transformation of ferrihy-drite in the presence or absence of trace Fe(II): the effect of preparation procedures of ferrihydrite. J Solid State Chem 182:1767–1771

Lovley D, Phillips E (1986) Organic-matter mineralization with reduction of ferric iron in anaerobic sediments. Appl Environ Microbiol 51:683–689 [PubMed: 16347032]

Lu L, Li LP, Wang XJ, Li GS (2005) Understanding of the finite size effects on lattice vibrations and electronic transitions of nano alpha-Fe_2O_3. J Phys Chem B 109:17151–17156 [PubMed: 16853187]

Maich AA, Erdem EY, Doyle FM (2012) Characterization of magnetic and non-magnetic iron oxide nanoparticles synthesized by different routes In: Hwang JY, Monteiro SN, Bai CG, Carpenter J, Cai M, Firrao D, Kim BG (eds) Characterization of minerals, metals, and materials. Wiley, New York, pp 99–106

Maiti D, Devi PS (2015) Selective formation of iron oxide and oxy-hydroxide nanoparticles at room temperature: critical role of concentration of ferric nitrate. Mater Chem Phys 154:144–151

Maity D, Agrawal DC (2007) Synthesis of iron oxide nanoparticles under oxidizing environment and their stabilization in aqueous and non-aqueous media. J Magn Magn Mater 308:46–55

Mcmillan P (1984) Structural studies of silicate-glasses and melts—applications and limitations of Raman-spectroscopy. Am Miner 69:622–644

McMillan PF, Hofmeister A (1988) Infrared and Raman spectroscopy. Rev Mineral 18:99–159

Michel FM, Ehm L, Liu G, Han WQ, Antao SM, Chupas PJ, Lee PL, Knorr K, Eulert H, Kim J et al. (2007) Similarities in 2- and 6-line ferrihydrite based on pair distribution function analysis of X-ray total scattering. Chem Mater 19:1489–1496

Mohammadikish M (2014) Hydrothermal synthesis, characterization and optical properties of ellipsoid shape alpha-Fe_2O_3 nanocrystals. Ceram Int 40:1351–1358

Mohapatra M, Mohapatra L, Anand S, Mishra BK (2010) One-pot synthesis of high surface area nano-akaganéite powder and its cation sorption behavior. J Chem Eng Data 55:1486–1491

Morris R, Lauer H (1990) Matrix effects for reflectivity spectra of dispersed nanophase (superparamagnetic) hematite with application to Martian spectral data. J Geophys Res Solid 95:5101–5109

Morris R, Lauer H, Lawson C, Gibson E, Nace G, Stewart C (1985) Spectral and other physicochemical properties of submicron powders of hematite (alpha-Fe_2O_3), maghemite (gamma-Fe_2O_3), magnetite (Fe_3O_4), goethite (alpha-FeOOH), and lepidocrocite (gamma-FeOOH). J Geophys Res Solid 90:3126–3144

Morris R, Agresti D, Lauer H, Newcomb J, Shelfer T, Murali A (1989) Evidence for pigmentary hematite on Mars based on optical, magnetic, and Mössbauer studies of superparamagnetic (nanocrystalline) hematite. J Geophys Res-Solid 94:2760–2778

Morris RV, Lauer HV, Schulze DG, Burns RG (1991) Preparation and characterization of a nanophase hematite powder. In: Proceedings of the 22nd lunar and planetary science conference, 1462

Morris RV, Golden DC, Bell JF (1997) Low-temperature reflectivity spectra of red hematite and the color of Mars. J Geophys Res Planet 102:9125–9133

Morris RV, Golden DC, Bell JF, Shelfer TD, Scheinost AC, Hinman NW, Furniss G, Mertzman SA, Bishop JL, Ming DW et al. (2000) Mineralogy, composition, and alteration of Mars Pathfinder rocks and soils: evidence from multispectral, elemental, and magnetic data on terrestrial analogue, SNC meteorite, and Pathfinder samples. J Geophys Res Planet 105:1757–1817

Morris RV, Klingelhöfer G, Schröder C, Rodionov DS, Yen A, Ming DW, de Souza PA, Wdowiak T, Fleischer I, Gellert R et al. (2006) Mössbauer mineralogy of rock, soil, and dust at Meridi-ani Planum, Mars: opportunity's journey across sulfate-rich outcrop, basaltic sand and dust, and hematite lag deposits: iron mineralogy at Meridiani Planum. J Geophys Res Planet 111:E12S15. doi:10.1029/2006JE002791

Murad E (1979) Mössbauer and x-ray data on beta-FeOOH (akagane-ite). Clay Miner 14:273–283

Murad E, Bishop JL (2000) The infrared spectrum of synthetic aka-ganeite, beta-FeOOH. Am Mineral 85:716–721

Nasdala L, Smith DC, Kaindl R, Zieman MA (2004) Raman spectroscopy; analytical perspectives in mineralogical research. EMU Notes Mineral 6:281–343

Navrotsky A, Mazeina L, Majzlan J (2008) Size-driven structural and thermodynamic complexity in iron oxides. Science 319:1635–1638 [PubMed: 18356516]

Oh SJ, Cook DC, Townsend HE (1998) Characterization of iron oxides commonly formed as corrosion products on steel. Hyperfine Interact 112:59–65

Pan C, Rogers AD, Thorpe MT (2015) Quantitative compositional analysis of sedimentary materials using thermal emission spectroscopy: 2. Application to compacted fine-grained mineral mixtures and assessment of applicability of partial least squares methods. J Geophys Res Planet 120:1984–2001

Pankhurst QA, Connolly J, Jones SK, Dobson J (2003) Applications of magnetic nanoparticles in biomedicine. J Phys D Appl Phys 36:R167–R181

Parikh SJ, Goyne KW, Margenot AJ, Mukome FND, Calderón FJ (2014) Soil chemical insights provided through vibrational spectroscopy In: Advances in Agronomy, vol 126 Elsevier, CA, USA, pp 1–147

Pérez-Pueyo R, Soneira MJ, Ruiz-Moreno S (2010) Morphology-based automated baseline removal for Raman spectra of artistic pigment. Appl Spectrosc 64:595–600 [PubMed: 20537226]

Rendón J, Serna C (1981) Ir-spectra of powder hematite—effects of particle-size and shape. Clay Miner 16:375–381

Risti M, Musi S, Godec M (2006) Properties of gamma-FeOOH, alpha-FeOOH and alpha-Fe_2O_3 particles precipitated by hydrolysis of Fe^{3+} ions in perchlorate containing aqueous solutions. J Alloy Compd 417:292–299

Roden EE (2003) Fe(III) oxide reactivity toward biological versus chemical reduction. Environ Sci Technol 37:1319–1324

Rout K, Mohapatra M, Layek S, Dash A, Verma HC, Anand S (2014) The influence of precursors on phase evolution of nano iron oxides/oxyhydroxides: optical and magnetic properties. New J Chem 38:3492

Ruan HD, Frost RL, Kloprogge JT (2001) The behavior of hydroxyl units of synthetic goethite and its dehydroxylated product hem-atite. Spectrochim Acta Acta 57:2575–2586

Ruppin R, Englman R (1970) Optical phonons of small crystals. Rep Prog Phys 33:14–196

Salisbury J, Wald A (1992) The role of volume scattering in reducing spectral contrast of reststrahlen bands in spectra of powdered minerals. Icarus 96:121–128

Šari A, Music S, Nomura K, Popovic S (1998) Microstructural properties of Fe-oxide powders obtained by precipitation from $FeCl_3$ solutions. Mater Sci Eng B Solid 56:43–52

Scheinost AC, Chavernas A, Barrón V, Torrent J (1998) Use and limitations of second-derivative diffuse reflectance spectroscopy in the visible to near-infrared range to identify and quantify Fe oxide minerals in soils. Clay Clay Miner 46:528–536

Scheinost AC, Schulze DG, Schwertmann U (1999) Diffuse reflectance spectra of Al substituted goethite: a ligand field approach. Clays Clay Miner 47:156–164. doi:10.1346/CCMN. 1999.0470205

Schulze D (1984) The influence of aluminum on iron-oxides. 8. Unit-cell dimensions of Al-substituted goethites and estimation of Al from them. Clay Clay Miner 32:36–44

Schwertmann U (1984a) The double dehydroxylation peak of goe-thite. Thermochim Acta 78:39–46

Schwertmann U (1984b) The influence of aluminum on iron-oxides. 9. Dissolution of Al-goethites. Clay Miner 19:9–19

Schwertmann U, Cornell RM (2000) Iron oxides in the laboratory: preparation and characterization, 2nd edn. Wiley, New York

Schwertmann U, Fischer W (1973) Natural amorphous ferric hydroxide. Geoderma 10:237–247

Schwertmann U, Cambier P, Murad E (1985) Properties of goethites of varying crystallinity. Clay Clay Miner 33:369–378

Serna CJ, Morales MP (2004) Maghemite (γ-Fe_2O_3): a versatile magnetic colloidal material In: Matijevic E, Borkovec M (eds) Surface and colloid science 17 Springer, New York, pp 27–81

Sherman D, Waite T (1985) Electronic-spectra of Fe-$^{3+}$ oxides and oxide hydroxides in the near Ir. Am Mineral 70:1262–1269

Sherman D, Burns R, Burns V (1982) Spectral characteristics of the iron-oxides with application to the Martian bright region mineralogy. J Geophys Res 87:169–180

Sheydaei M, Aber S (2013) Preparation of nano-lepidocrocite and an investigation of its ability to remove a metal complex dye. Clean Soil Air Water 41:890–898

Sklute EC, Kashyap S, Holden JF, Dyar MD (2016a) Spectral evolution of bioreduced ferrihydrite by hyperthermophiles. In: Proceedings from the biosignatures preservation and detection in mars analog environments conference, 2048

Sklute EC, Dyar MD, Kashyap S, Holden JF (2016b) The challenge of distinguishing iron (hydr)oxides and what it means for Mars. In: Geological society of america fall meeting, 197–10

Sobron P, Bishop JL, Blake DF, Chen B, Rull F (2014) Natural Fe-bearing oxides and sulfates from the Rio Tinto Mars analog site: critical assessment of VNIR reflectance spectroscopy, laser Raman spectroscopy, and XRD as mineral identification tools. Am Mineral 99:1199–1205

Soltis JA, Penn RL (2016) Oriented attachment and nonclassical formation in iron oxides In: Faivre D (ed) Iron oxides. Wiley, New York, pp 243–268

Stuart B (2004) Infrared spectroscopy: fundamentals and applications. Wiley, New York

Taylor R, Schwertmann U (1974) Maghemite in soils and its origin. 2. Maghemite syntheses at ambient-temperature and pH 7. Clay Miner 10:299–310

Vodyanitskii YN (2010) Iron hydroxides in soils: a review of publications. Eurasian Soil Sci 43:1244–1254

Wada SI, Ueno N (2001) Effect of monosilicic acid on hydrolytic polymerization of Fe(III) and structure of hydrolytic products. Soil Sci Plant Nutr 47:727–735

Wang L, Gao L (2010) Self-assembly behavior of hematite nanoparticles with controllable anisotropic morphology. J Colloid Interface Sci 349:519–526 [PubMed: 20584529]

Wartewig S (2003) IR and Raman spectroscopy: fundamental processing. Wiley, New York

Waychunas GA (2009) Natural nanoparticle structure, properties and reactivity from X-ray studies. Powder Diffr 24:89–93

Weckler B, Lutz HD (1998) Lattice vibration spectra. Part XCV. Infrared spectroscopic studies on the iron oxide hydroxides goethite (alpha), akaganéite (beta), lepidocrocite (gamma), and feroxyhite (delta). Eur J Solid State Inorg 35:531–544

Wenrich ML, Christensen PR (1996) Optical constants of minerals derived from emission spectroscopy: application to quartz. J Geophys Res Sol Ea 101:15921–15931

Wigginton NS, Haus KL, Hochella MF, Jr (2007) Aquatic environmental nanoparticles. J Environ Monit 9:1306 [PubMed: 18049768]

Wolska E, Schwertmann U (1989) Selective x-ray-line broadening in the goethite-derived hematite phase. Phys Status Solidi A 114:K11–K16

Yariv S, Mendelovici E (1979) Effect of degree of crystallinity on the infrared-spectrum of hematite. Appl Spectrosc 33:410–411

Zeng S, Tang K, Li T (2007) Controlled synthesis of α-Fe$_2$O$_3$ nanorods and its size-dependent optical absorption, electro-chemical, and magnetic properties. J Colloid Interface Sci 312:513–521 [PubMed: 17498731]

Zhang H, Bayne M, Fernando S, Legg B, Zhu M, Penn RL, Banfield JF (2011) Size-dependent bandgap of nanogoethite. J Phys Chem C 115:17704–17710

Zhang X, Niu Y, Li Y, Hou X, Wang Y, Bai R, Zhao J (2013) Synthesis, optical and magnetic properties of alpha-Fe$_2$O$_3$ nanoparticles with various shapes. Mater Lett 99:111–114

Zhang Y, Yan P, Wan Q, Wu K, Yang N (2016) Morphology-dependent electrochemistry of FeOOH nanostructures. Electrochem Com-mun 68:10–14

Zhong W, Du Y (2003) Magnetic liquids In: Liu Y, Zhang Z, Wang ZL (eds) Handbook of nanophase and nanostructured materials. Springer, New York, pp 1065–1101

Žic M, Risti M, Music S (2007) Fe-57 Mössbauer, FT-IR and FE SEM investigation of the formation of hematite and goethite at high pH values. J Mol Struct 834:141–149
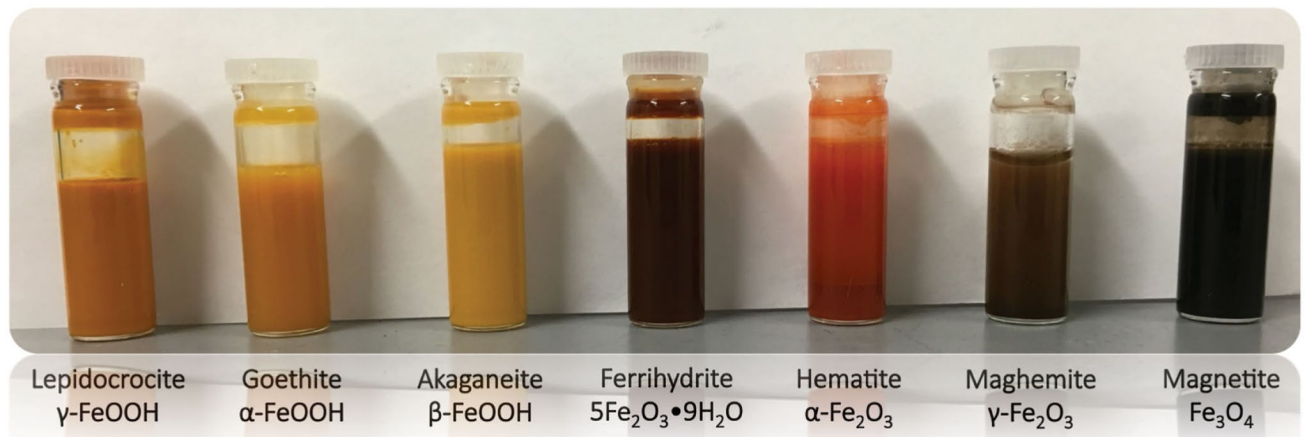
Fig. 1.
Suspensions of representative samples for each mineral
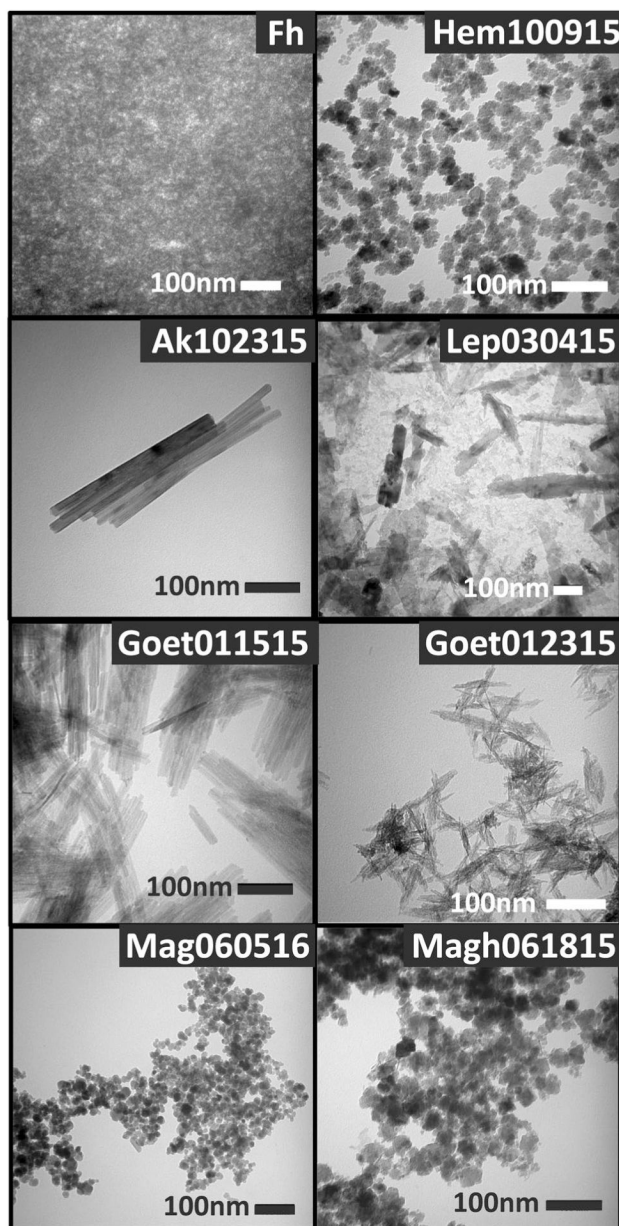
Fig. 2.
TEM of samples used in this study. Note the dramatic difference in crystallinity between the two goethite syntheses, despite quite similar sizes. The *scale bar* in all cases is 100 nm. Note that the particle sizing results were acquired over multiple frames for a total of 100 or more particles and these images may not reflect the full distribution
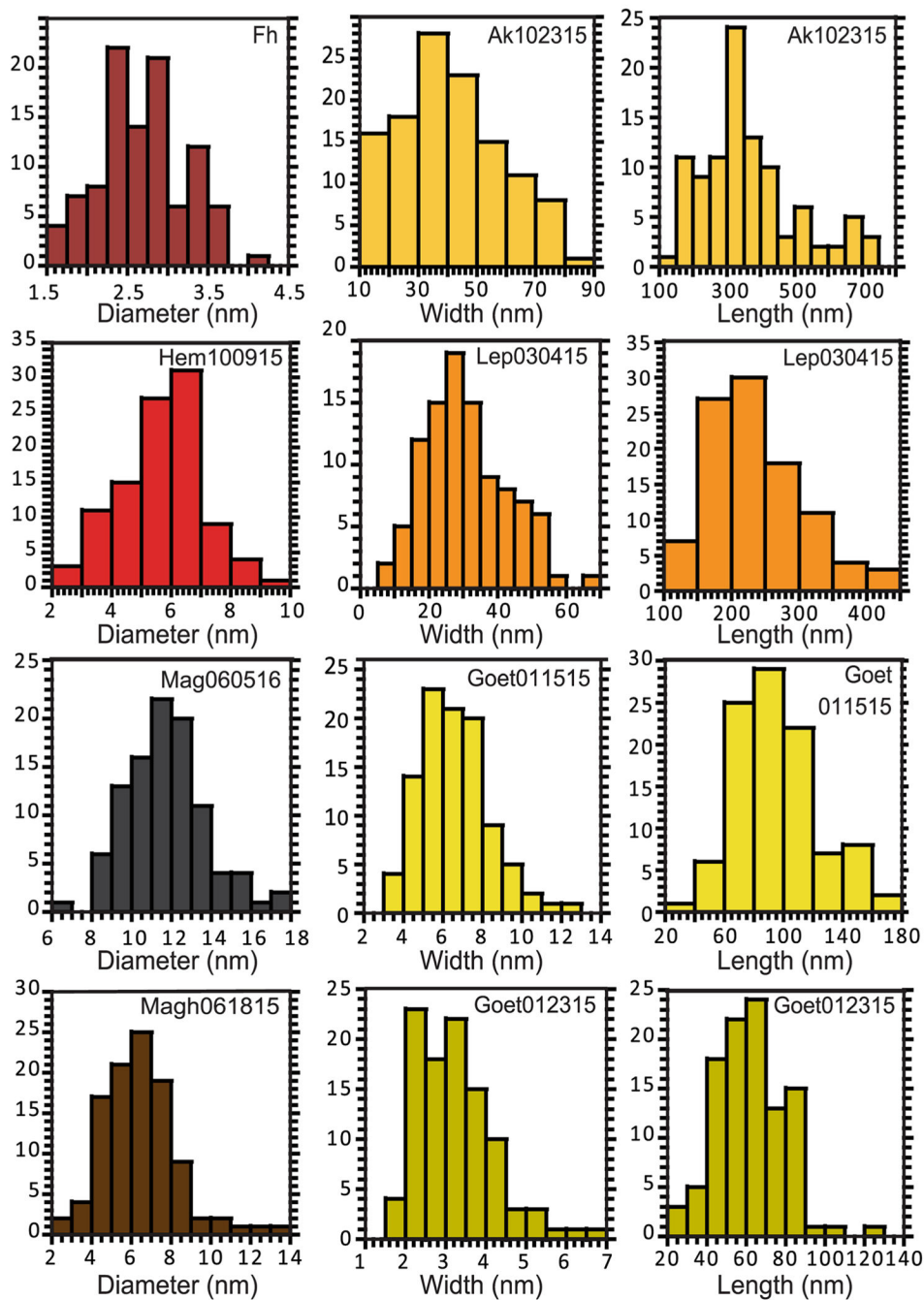
Fig. 3.
Particle sizing results for width/diameter and length of iron NPOs obtained from TEM analysis. The particle sizes are given for individual particles, although aggregates may be larger. Diameters of spherical samples are shown on the *left,* widths of acicular/tabular samples are shown in the *center,* and lengths of acicular/tabular samples are shown on the *right*
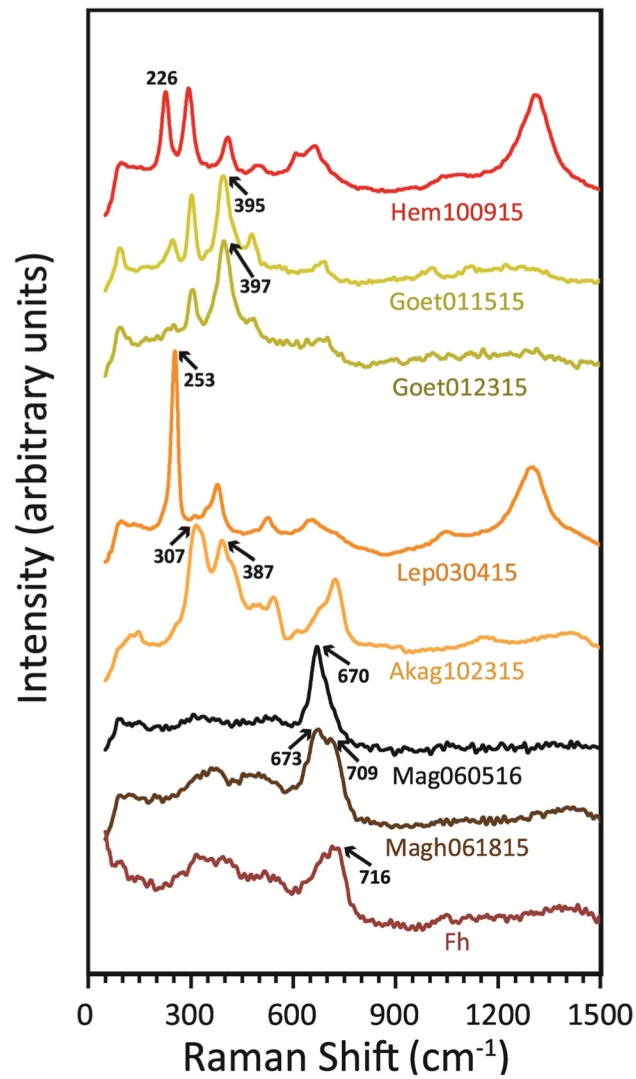
Fig. 4.
Raman spectra of Iron NPOs. Spectra are scaled and offset for clarity. Raman features used for identification (bold, underlined values in Table 2) are indicated on the plot. Note the subtle spectral change between the two goethite samples and the overlapping peak positions for magnetite, maghemite, and ferrihydrite
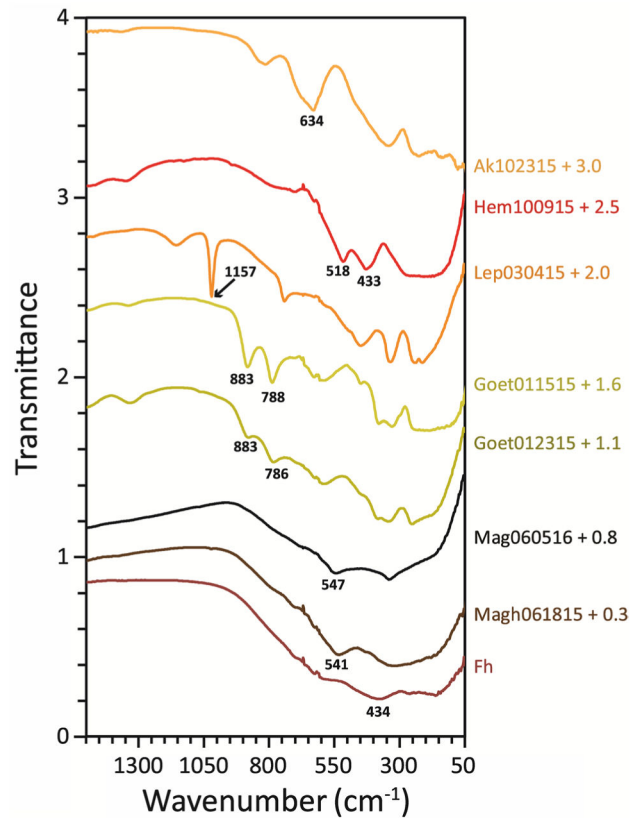
Fig. 5.
FTIR ATR spectra of nanophase iron oxides. Spectra are offset by amount indicated. MIR features used for identification (bold, underlined values in Table 3) are indicated on the plot. Note the overlapping peak positions for magnetite and maghemite
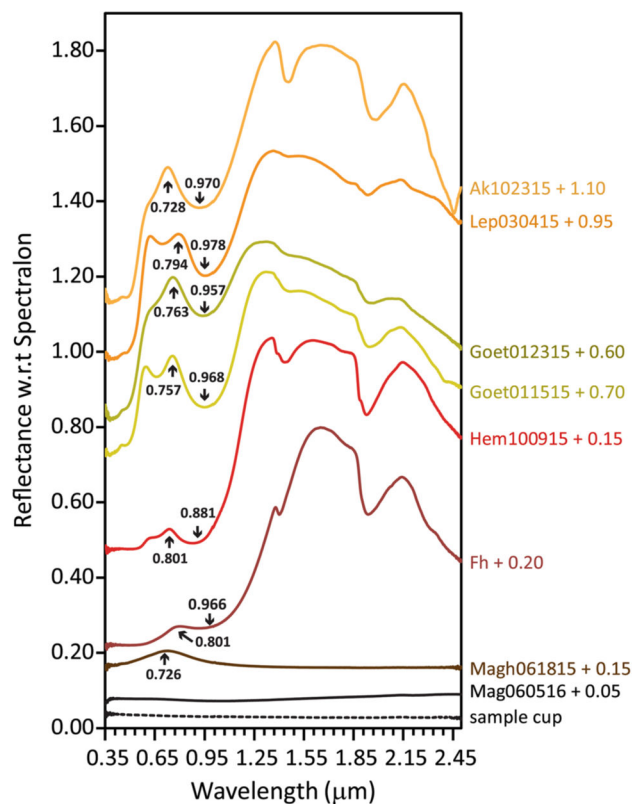
Fig. 6.
VNIR spectra of nanophase iron oxides. Spectra are offset by amount indicated. The position of the $^6A_1 \rightarrow {}^4T_1$ transition as well as the VIS spectral maximum are indicated for each sample as these can often be used for mineral differentiation. Note that magnetite and maghemite can be easily differentiated by their VNIR spectra; however, this distinction may be lost in mixed-phase samples

Table 1

Crystallographic and physical parameters for synthetic iron NPOs

Sample	Mineral	Formula	Crystal system	Space group	Grain shape	Width (nm)	Length (nm)
Fh	Ferrihydrite	$5Fe_2O_3.9H_2O$	Hexagonal	$P6_3mc$	Sphere	3 ± 1	-
Goet011515	Goethite	$\alpha\text{-FeOOH}$	Orthorhombic	Pnma	Lathe	7 ± 2	96 ± 28
Goet012315	Goethite	$\alpha\text{-FeOOH}$	Orthorhombic	Pnma	Lathe	3 ± 1	62 ± 18
Ak102315	Akaganéite	$\beta\text{-FeOOH}$	Monoclinic	I2/m	Lathe	41 ± 17	367 ± 143
Lep030415	Lepidocrocite	$\gamma\text{-FeOOH}$	Orthorhombic	$Cmc2_1$	Platelet	31 ± 12	237 ± 72
Hem100915	Hematite	$\alpha\text{-Fe}_2O_3$	Trigonal	R3c	Sphere	6 ± 1	-
Magh061815	Maghemite	$\gamma\text{-Fe}_2O_3$	Cubic	$P4_132$	Irregular	6 ± 2	-
Mag060516	Magnetite	Fe_3O_4	Cubic	Fd3m	Sphere	12 ± 2	-

Table 2

Raman shift peak positions (cm^{-1}) with those reported for bulk iron (oxyhydr) oxides

Hem100915	226		294	408	493	608	663
α-Fe$_2$O$_3$[a]	**225**	245	291	411	500	611	661
Symmetry[b,c,d] Species[b]	A_{1g} Fe–O	E_g Fe–O	E_g Fe–O	E_g Fe–O	A_{1g}	E_g Fe–O	LO E_u
Goet011515	247	303	395	480			665/686
Goet012315	250	305	397	471,483			686
α-FeOOH[a]	244	299	**385**	480	548		681
Symmetry[e] Species[e]	A_{1g} Fe–O	E_g Fe–OH	E_g Fe–O/–OH	A_g Fe–OH	–Fe–OH		–Fe–O
Lep030415	253		378		527	648	
γ-FeOOH[a]	**250**	348	379		528	650	
Ak102315	146	316	391		546	614	723
β-FeOOH[f]	137	**307**	**387**		535	597	719
Mag060516						670	
Fe$_3$O$_4$[a]		310			540	**670**	
Symmetry[b] Species[b]		T_{2g} O			T_{2g} Fe$_A$–O	A_{1g} O	
Magh061815						673	709
γ-Fe$_2$O$_3$[a]			350		512	**665**	**730**
Symmetry[b] Species[b]			T_1 Fe–O		E Fe–O	A_1 Fe–O	
Fh						716	
5Fe$_2$O$_3$.9H$_2$O[g]			361		508	**707**	

Bold, underlined values are considered diagnostic features. Site symmetries and participating atoms are listed where known

The precision of the determined peak location exceeds common reporting practices for Raman peak positions; errors are, therefore, not included in this table

LO longitudinal

[a] Hanesch (2009)

[b] Chamritski and Burns (2005) and references therein

[c] Bersani et al. (1999)

[d] Jubb and Allen (2010)

[e] Rout et al. (2014)

[f] Das and Hendry (2011)

[g] Das et al. (2013)

Table 3

MIR peak positions (cm⁻¹) along with those reported for bulk iron (oxyhydr)oxides

Sample	≥1000	770–900	695–760	640–690	595–635	540–590	497–530	447–496	409–446	355–400	310–354	265–300	210–264
Hem100915	1157	779	706	664	628, 604s		518		433			279	
α-Fe₂O₃^{a,b,c}			700^b				**525**^{a}		**443**^{a}	~380–400^c	~335–310^c		229^c
Origin^{a,b,c}			Fe–OH				E_u / Fe–O		A_{2u} / Fe–O	E_u / Fe–O	A_{2u} / Fe–O		E_u / Fe–O
Goet011515	883	788		671	629	590, 483s		450		382	334	298s	249
Goet012315	883	786	697s	671, 663s	626	590, 486s		447		392	342	297s	256
α-FeOOH^a		839, **794**		670	633		497	450	409	361		268	
Origin^{d,e}	B_{2u}, δ$_{OH}$	B_{1u}, γ$_{OH}$		δ$_{OH}$	ν$_{Fe–O}$	ν$_{Fe–O}$asym	ν$_{Fe–O}$		ν$_{Fe–O}$asym	ν$_{Fe–O}$sym		ν$_{Fe–O}$sym	
Lep030415	1020		741	669	629	583	507s	452			338		245, 217
γ-FeOOH^f	**1150**, **1018**		752		610		510	478		357		270	223
Origin^f	B_{2u}, δ$_{OH}$	B_{3u}	B_{1u}, δ$_{OH}$		B_{3u}		B_{2u}, τ$_O$	τ$_{OH}$		B_{2u}		B_{1u}	B_{3u}
Ak102315	837, 816		677s		634			469s	416s	363			252, 224
β-FeOOH^g	845s, 817		**698**	**644s**		**560**, **553**		470s	422				
Origin^g	δ$_{OH}$		δ$_{OH}$			T_{1u}, T_2		Fe–O	Fe–O				
Mag060516						547					346		
Fe₃O₄^c						**560**					350		210
Origin^c						T_{1u} / Fe–O				T_{1u} / Fe–O		T_{1u} / Fe–O	
Magh061815		773s, 706				541			433		343		252
γ-Fe₂O₃^c						**553**			440		319	270	
Origin^c						T_2 / Fe–O			T_2 / Fe–O		T_2		Fe–O
Fh		698			602				434			278	
5Fe₂O₃·9H₂O^e		650						**450**					

Origin[e]	def_{OH}	def_{OH}

Bold, underlined values are considered diagnostic features. Site symmetries and participating atoms are listed where known

Errors in peak positions are smaller than the resolution of the measurement (4 cm^{-1}) but can vary substantially with continuum removal method. See text for details

def deformation, *asym* asymmetric, *sym* symmetric, *s* shoulder

[a] Parikh et al. (2014)

[b] Barrón et al. (2003)

[c] Chamritski and Burns (2005) and references therein

[d] Blanch et al. (2008)

[e] Cornell and Schwertmann (2006)

[f] Lewis and Farmer (1986)

[g] Murad and Bishop (2000); Bishop et al. (2015)

Table 4

VNIR peak positions

Mineral												
Hem100915			0.537		0.672	0.881	1.003	1.428	1.795	1.935		
α-Fe_2O_3[a]	0.380	0.404	0.444	0.529	0.649	0.884						
Origin[b,c]	$^6A_1\to{}^4E$	$^6A_1\to{}^4T_2$	$^6A_1\to{}^4E\,{}^4A_1$	$2(^6A_1\to{}^4T_1)$	$^6A_1\to{}^4T_2$	$^6A_1\to{}^4T_1$				OH/H_2O comb		
Goet011515	0.374		0.484		0.678	0.968		1.449	1.774	1.940	2.332	2.397
Goet012315	0.395		0.485		0.675	0.957		1.446	1.777	1.940		
α-FeOOH[a]	0.364	0.434	0.480		0.649	0.917						
Origin[b,c]	$^6A_1\to{}^4E$		$^6A_1\to{}^4E\,{}^4A_1$	$2(^6A_1\to{}^4T_1)$	$^6A_1\to{}^4T_2$	$^6A_1\to{}^4T_1$		OH stretch ot		OH/H_2O comb		
Lep030415	0.414		0.482		0.726	0.978		1.453	1.818	1.930	2.207	2.477
γ-FeOOH[a]	0.359	0.434	0.485		0.649	0.961						
Origin[b,c]	$^6A_1\to{}^4E$		$^6A_1\to{}^4E\,{}^4A_1$	$2(^6A_1\to{}^4T_1)$	$^6A_1\to{}^4T_2$	$^6A_1\to{}^4T_1$				OH/H_2O comb		
Ak102315	0.387	0.428	0.512		0.650	0.970		1.456		1.966	2.324	2.452
β-FeOOH[b,d]				0.502[b]		0.908[b]		1.458[d]		1.984[d]	2.324[d]	2.457[d]
Origin[b,d]				$2(^6A_1\to{}^4T_1)$		$^6A_1\to{}^4T_1$		OH, H_2O stretch ot		H_2O comb	OH cb	OH cb
Mag060516							1.049	1.400				
Fe_3O_4[a]												
Origin[b]							CT					
Magh061815			0.472									
γ-Fe_2O_3[a]		0.434	0.510		0.666	0.934						
Origin[b]			$^6A_1\to{}^4E\,{}^4A_1$	$2(^6A_1\to{}^4T_1)$	$^6A_1\to{}^4T_2$	$^6A_1\to{}^4T_1$						
Fh						0.966		1.403	1.796	1.933	2.296	
$5Fe_2O_3\cdot9H_2O$[e]	0.410		0.492		0.716	0.972						
Origin[c,e]	$^6A_1\to{}^4E$		$^6A_1\to{}^4E\,{}^4A_1$	$2(^6A_1\to{}^4T_1)$	$^6A_1\to{}^4T_2$	$^6A_1\to{}^4T_1$		OH stretch ot		OH/H_2O comb		

Site symmetries and participating atoms are listed where known

Errors in peak positions are smaller than the resolution of the measurement (3 nm) but can vary substantially with continuum removal method. See text for more details

CT charge transfer, *ot* overtone, *cb* combination band

NASA Author Manuscript

[a]Sherman and Waite (1985)

[b]Cornell and Schwertmann (2006)

[c]Hunt et al. (1971)

[d]Bishop et al. (2015)

[e]Scheinost et al. (1998)

NASA Author Manuscript

NASA Author Manuscript